Role of variability in determining the vertical wind speeds and structure

Erdal Yiğit[1] and Aaron J. Ridley[1]

Received 31 March 2011; revised 30 August 2011; accepted 23 September 2011; published 6 December 2011.

[1] The University of Michigan's Global Ionosphere Thermosphere Model (GITM) is used to study the temporal and spatial variability of high-latitude vertical winds during the December solstice. Underlying mechanisms controlling the high-latitude distribution and the magnitude of vertical winds in the thermosphere are investigated in a suite of systematic model simulations. First, in a series of six model simulations GITM longitude × latitude resolution is gradually increased from 5° × 5° to 2.5° × 0.3125°, imposing constant moderate solar and low magnetospheric activity in all simulations. Analysis of the high-latitude mean parameters shows that polar distributions of vertical winds and Joule heating demonstrate localized enhancements at high spatial resolution that are not well captured at coarse grid resolution. Second, in simulations with fixed spatial resolution of 2.5° × 2.5°, the impact of temporally variable magnetospheric conditions on the morphology of the high-latitude vertical winds has been investigated. For this, hemispheric power and the cross polar cap potential values are modified in a series of systematic simulations. The magnitude and temporal variations of ion flows significantly impact the high-latitude Joule heating, which in turn dramatically effects the vertical wind structure. It is demonstrated that variability in the vertical winds are driven by variability in the ion flows and that sudden step-like changes in ion flows can cause the largest enhancements in the vertical winds, in particular, via nonhydrostatic effects. The vertical wind variability is seen to be the largest in the summer Southern Hemisphere with much larger vertical wind magnitudes.

Citation: Yiğit, E., and A. J. Ridley (2011), Role of variability in determining the vertical wind speeds and structure, *J. Geophys. Res.*, *116*, A12305, doi:10.1029/2011JA016714.

1. Introduction

[2] The thermosphere-ionosphere (TI) system, extending from ∼100 km upwards to approximately 1000 km, demonstrates a significant degree of vertical coupling, upward from the lower atmosphere and downward from the magnetosphere. Increasing number of observations suggest that large vertical winds are continuously present in the thermosphere [*Spencer et al.*, 1976, 1982; *Rees et al.*, 1984; *Wardill and Jacka*, 1986; *Crickmore et al.*, 1991; *Price et al.*, 1995; *Innis et al.*, 1999; *Ishii et al.*, 2001]. Large upwelling events are found to be well correlated with the occurrence of geomagnetic storms and lead to dramatic temperature variations within a few minutes [*Price et al.*, 1995]. Global observations conducted with the Wind and Temperature Spectrometer on the Dynamics Explorer-2 satellite highlight large local time variations of vertical winds, indicating enhanced vertical wind variability in/near the polar cap [*Innis and Conde*, 2001]. *Innis and Conde* [2002] have also studied gravity wave generation using satellite observations of vertical winds in the thermosphere. Underlying dynamical and thermal mechanisms for vertical wind generation are discussed to some extent in the works by *Smith* [1998] and *Smith* [2000]. Some researchers attributed measured vertical winds at midlatitudes to horizontal wind divergences [*Biondi*, 1984] and the passage of atmospheric gravity waves [*Hernandez*, 1982; *Sakanoi and Fukunishi*, 1999]. Enhanced vertical winds can generate a net transport of chemical constituents across levels of constant pressure, which may create additional variability of atmospheric composition. Compositional changes induced by vertical winds can then be transported horizontally by prevailing winds [*Rishbeth*, 1998], having global-scale effects. Historically, based on the assumption of hydrostatic equilibrium, most general circulation models (GCMs) that are extending into the upper atmosphere [e.g., *Roble et al.*, 1988; *Richmond et al.*, 1992] produce vertical winds that are relatively small with respect to the horizontal winds and thus observed mean vertical winds are typically not well captured by models based on hydrostatic equilibrium [*Conde and Dyson*, 1995].

[3] Temporal and spatial variability of thermospheric vertical winds is thought to be a complex function of several

[1]Center for Space Environment Modeling, Department of Atmospheric, Oceanic and Space Sciences, University of Michigan, Ann Arbor, Michigan, USA.

0148-0227/11/2011JA016714

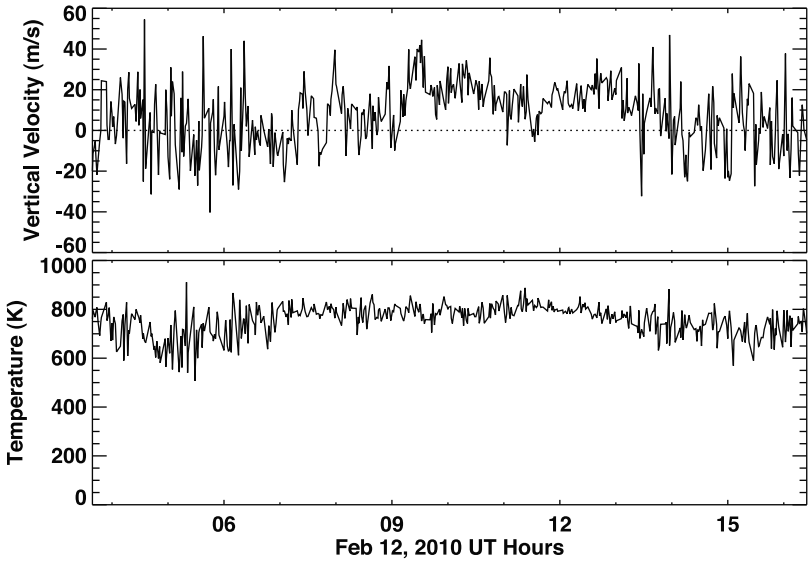

Figure 1. (top) The vertical wind and (bottom) temperature at Poker Flat Alaska at roughly 240 km altitude measured by a Fabry-Perot Interferometer on February 12, 2010.

neutral and electrodynamic processes that take place at various scale sizes in terms of space and time. To study vertical winds in a highly energetic upper atmosphere environment, several dynamical and thermal processes should thus be considered. Momentum deposition associated with ion-neutral coupling, i.e., ion drag [*Killeen and Roble*, 1984; *Killeen et al.*, 1991] significantly shape the general circulation. The resulting frictional heating is an important source of energy for the high-latitude thermosphere-ionosphere [*Wilson et al.*, 2006; *Yiğit and Ridley*, 2011], constituting a significant portion of the electromagnetic energy deposited into the ionosphere [*Thayer et al.*, 1995; *Thayer and Semester*, 2004]. The orientation and the magnitude of the interplanetary magnetic field (IMF) has a great impact on the morphology of the high-latitude Joule heating [*McHarg et al.*, 2005] and the ionospheric convection patterns at high-latitudes [*Heelis*, 1984; *Knipp et al.*, 1991; *Ridley et al.*, 1998]. The thermosphere-ionosphere system is also controlled from below. Recent studies indicate the dynamical and thermal importance of small-scale gravity waves of lower atmosphere origin [*Yiğit et al.*, 2009; *Yiğit and Medvedev*, 2009] based on the extended nonlinear gravity wave parameterization by *Yiğit et al.* [2008]. Complex interplay of lower atmospheric and magnetospheric effects make the upper atmosphere a challenging region to study and it is therefore crucial to use GCMs to conduct sensitivity and diagnostic studies to advance our understanding of coupling processes.

[4] Figure 1 shows vertical wind and temperature measurements from a Fabry-Perot Interferometer at an auroral zone station during winter time. The main features to note in Figure 1 are that there are time periods in which the vertical wind is quite large (20 m s^{-1}) for over an hour and that there is significant temporal variability in the vertical wind, with significant bi-polar signatures, indicative of wave-like structure. While this paper does not seek to explain the exact features observed during this time period, it does attempt to explain a possible reason for the existence of the large vertical wind variability.

[5] In this research paper, we analyze qualitatively the temporal and spatial variability of neutral vertical winds in the high-latitude thermosphere associated with (1) increasing model spatial resolution and (2) variable ion flows. To identify possible mechanisms that control the overall morphology of the high-latitude vertical winds, we primarily focus on the analysis of the heat sources associated with particle precipitation and Joule dissipation of magnetospheric origin at low geomagnetic activity at varying spatial resolution and at geomagnetically disturbed conditions at a fixed resolution. The overarching science goal is thus to advance the current understanding of spatial and temporal structures of vertical winds and dynamical mechanisms that contribute to their variability.

[6] Section 2 introduces the Global Ionosphere Thermosphere Model, section 3 describes the model setup and the associated configurations of runs to study the science questions. Model results are presented and discussed in sections 4–5. Summary and conclusions are given in section 6.

2. Model Description

[7] The University of Michigan Global Ionosphere-Thermosphere Model (GITM) is a 3-D first principle nonhydrostatic general circulation model (GCM) and is fully described in the work by *Ridley et al.* [2006]. GITM extends from ~100 km to ~650 km, depending on the solar activity. Model vertical variations are represented in the altitude coordinate system, instead of the pressure coordinate system traditionally used in thermosphere models [e.g., *Fuller-Rowell and Rees*, 1980; *Dickinson et al.*, 1981; *Richmond et al.*, 1992]. The vertical momentum equation is explicitly solved, thus allowing the model to account for nonhydrostatic vertical motions that are associated with vertical acceleration. *Deng et al.* [2008] have studied the nonhydrostatic motion in GITM and have found that it plays an

Table 1. GITM Simulations of Increasing Model Spatial Resolution (I)–(VI)[a]

Run	Longitude × Latitude
(I)	5° × 5°
(II)	5° × 2.5°
(III)	2.5° × 2.5°
(IV)	2.5° × 1.25°
(V)	2.5° × 0.625°
(VI)	2.5° × 0.3125°

[a]Note that (I) corresponds to a spatial horizontal scale of around 275 km × 550 km (at 60°N/S), while the highest resolution (VI) corresponds to 137.5 km × 35 km.

important role during intensive high-latitude Joule heating events. For this, the hydrostatic assumption

$$\frac{\partial p}{\partial r} = -\rho g, \tag{1}$$

is replaced by the vertical momentum equation

$$\frac{Dw_n}{Dt} = -\frac{1}{\rho}\frac{\partial p}{\partial r} + g + a_{cor} + a_{in} + a_{nn} + a_{sph}. \tag{2}$$

In the above equations, r is the radial distance from the center of the Earth, p is pressure, t is time, g is gravitational acceleration, $\frac{D}{Dt} = \frac{\partial}{\partial t} + \mathbf{u_n} \cdot \nabla$ is the material derivative with the three-dimensional neutral flow $\mathbf{u_n} = (u_n, v_n, w_n)$, and ρ is neutral mass density. The vertical acceleration terms, a_i, are as the following: a_{cor} includes acceleration due to centrifugal forces and Coriolis effects, a_{in} represents vertical ion drag, a_{nn} is neutral-neutral coupling, and a_{sph} accounts for the spherical geometry. Equation (2) will be further investigated in section 5.4. Accordingly, ion motion will be defined by $\mathbf{u_i} = (u_i, v_i, w_i)$ and the ion and neutral horizontal flow by $\mathbf{u_{i_H}} = (u_i, v_i)$ and $\mathbf{u_{n_H}} = (u_n, v_n)$, respectively.

[8] The model resolution is flexible and the time step can typically vary between 2 s and 4 s. This is one of the unique features of GITM, as most GCMs extending into the upper atmosphere have time steps of 30–60 s [e.g., *Fuller-Rowell and Rees*, 1980; *Yiğit et al.*, 2009]. The HAMMONIA model uses a time step of 10 min [*Schmidt et al.*, 2006] that can simulate variations on long timescales.

[9] A nonuniform grid can be used in altitude and/or latitude, which is helpful, for example, for studying high-latitude dynamics under highly disturbed geomagnetic and solar conditions. In our simulations, we use a uniform horizontal grid and 50 altitude levels in roughly 1/3 scale height separations.

[10] Lower boundary conditions are specified in two altitude "ghost cells" below the first physical altitude level (100 km), approximately corresponding to 96 km and 98 km. In the thermosphere, these cells are specified using MSISE-90 [*Hedin*, 1991]. For the high-latitude dynamics, a number of different models can be used. In this study, the high-latitude electric field patterns are obtained from the *Weimer* [1996] model and the particle precipitation is after the work by *Fuller-Rowell and Evans* [1987].

[11] Neutral densities of O, O_2, $N(^2D)$, $S(^2P)$, N_2, and NO; and ion species $O^+(^2P)$, O_2^+, N^+, $O^+(^4S)$, $O^+(^2D)$, N_2^+, and NO^+ are explicitly calculated. GITM has been recently used successfully to study various aspects of space physics [e.g., *Deng and Ridley*, 2007; *Yiğit and Ridley*, 2011].

3. Model Setup and Configuration of Runs

[12] Extensive flexibility in model spatial grid enables GITM to be run at any spatial resolution. Also, a very fine time step of 2–4 s provides high intrinsic variability, enabling detailed studies of the temporal variability of high-latitudes although typically the auroral and electric potential patterns are only updated every minute.

3.1. Variations of Model Spatial Resolution

[13] In order to test the effects of increasing spatial resolution, GITM is run at the following longitude × latitude resolutions: (I) 5° × 5°; (II) 5° × 2.5°; (III) 2.5° × 2.5°; (IV) 2.5° × 1.25°; (V) 2.5° × 0.625°; (VI) 2.5° × 0.3125° as summarized in Table 1, where the lowest resolution run (I) has a longitude-latitude scale of 275 km × 550 km (at 60°N/S) and the highest resolution run corresponds to 137.5 km × 35 km. In these simulations, GITM is run for 2 days from 20 to 22 December 0000 UT, outputting every two hours. The instantaneous results (or model snapshots) are presented at the end of the 2-day period (i.e., 22 December 0000 UT). For the varying spatial resolution runs, in order to eliminate any variability of magnetospheric and solar origin, we keep the geomagnetic and solar activity at constant values: $F_{10.7} = 150 \times 10^{-22}$ W m^{-2} Hz^{-1} and HP = 1 GW. The IMF (interplanetary magnetic field) parameters are $B_z = -2$ nT and $B_y = 0$ nT. Solar wind speed is 400 km s^{-1}. The chosen configuration of simulations can thus reveal the degree of the importance of spatial resolution to better capturing the vertical wind structures.

3.2. Variations of Magnetospheric Energy Input

[14] For a fixed spatial resolution of 2.5° × 2.5° (III) that corresponds to a spatial scale of 137.5 km × 275 km (at 60°N/S), GITM is used to investigate the response of vertical winds to variable ion flows imposed by variable high-latitude energy inputs. In order to generate the baseline quiet conditions referred to as III_0, GITM is first run with the solar and geomagnetic activity described in section 3.1 from 22 December 0000 to 0800 UT, outputting every five minutes. Then, run III_0 is repeated with HP = 30 GW (III_{30GW}). In the rest of the runs to be described, the hemispheric power is kept at 30 GW and is thus skipped in the discussion for simplicity. For the next run, B_z is intensified to −6 nT and held constant (III_{-6}). The final two runs impose an oscillating step function with a 15-minute period (III_{-6}^{step}) and a sinusoidal 15-minute variation (III_{-6}^{sin}) on B_z, both with ±3 nT amplitudes in the 8-hour modeled time period. Figure 2 visualizes the variations of B_z, where the different runs are denoted by the different line styles. As the initial conditions are constant in all runs before 22 December 0000 UT only the period thereafter is shown, illustrated by different line styles. It is noteworthy that both the step-like and sinusoidal variations have similar structures overall, with the same frequency and amplitude of variations.

[15] While these types of variations of the IMF exist (although not as ideal as described here), typically the large-scale ionospheric potential cannot respond to such high frequency variations such as these.

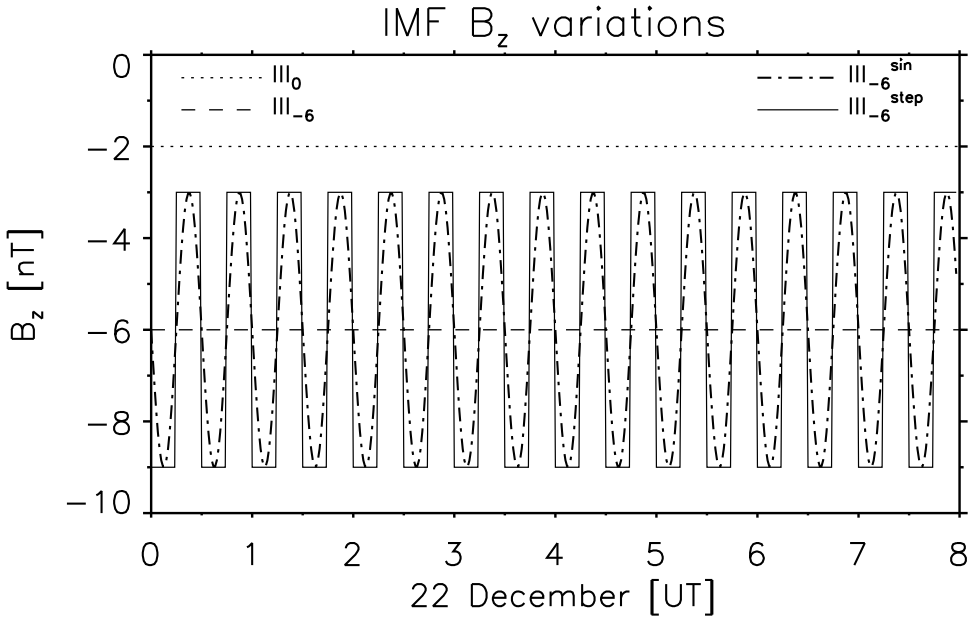

Figure 2. Variations of B_z [nT] in GITM, starting on 22 December 0000 UT for a period of 8 hours. Note that B_z has been kept constant in all runs prior to the period shown. Solar activity is at moderate constant level: $F_{10.7} = 150 \times 10^{-22}$ W m^{-2} Hz^{-1}. HP is 30 GW.

[16] Other studies have shown that the localized ion flow is quite variable, changing very quickly in both space [*Kivanç and Heelis*, 1998] and time [*Bristow*, 2008]. The variations that are imposed in our simulations are intended to illustrate static ion flows (III_0, III_{30GW}, III_{-6}), relatively quickly varying ion flows (III_{-6}^{sin}), and rapidly varying ion flows (III_{-6}^{step}). They are not meant to represent rapidly varying IMF conditions, but merely changing ion flow conditions that may be obscured in the auroral oval or during events such as substorms. Empirical models of the ion flows typically do not include dynamically changing flows for static IMF conditions, which is why the IMF is modulated.

3.3. Averaging Processes

[17] For the runs of increasing spatial resolution, the high-latitude area-weighted mean of a parameter X, $\langle X \rangle$, has been evaluated poleward of 50°N/S geographic latitudes and is a 24-hour mean (i.e., 21–22 December), based on 2-hour outputs. In the varying magnetospheric condition runs, the associated averaging has been performed over outputs of 15 min from 22 December 0000 to 0800 UT. All UT plots are based on a 5-minute output data set between 0000 and 0800 UT on 22 December.

4. Effects of Increasing Model Spatial Resolution

4.1. Global Mean High-Latitude Parameters

[18] In order to assess the impact of increasing model spatial resolution, the high-latitude means of some fundamental thermospheric parameters are evaluated. Figure 3 demonstrates the altitude variations of the combined Northern and Southern Hemisphere high-latitude mean zonal (Figure 3a), meridional (Figure 3b), and vertical (Figure 3c) wind magnitudes. Figures 3d–3f present the associated results for the zonal electric field magnitude, Joule (Q_J) and auroral heating (Q_A), respectively. Note that Joule and auroral heating refer to neutral gas heating rates in K s^{-1} resulting from Joule dissipation and particle heating, respectively. The change in Joule heating rate with resolution is discussed in substantial detail by *Yiğit and Ridley* [2011].

[19] The high-latitude mean neutral winds increase at all altitudes with increasing spatial resolution. Longitudinal resolution does not appear to have a large impact on the high-latitude mean of these variables while the latitudinal resolution plays a crucial role in the mean magnitudes. Peak magnitudes are found in the upper thermosphere. For example, vertical mean wind is up to ∼2 m s^{-1} at around 400 km. Horizontal winds play an important role in shaping vertical motion in the atmosphere through their divergences [*Biondi*, 1984; *Smith*, 1998].

[20] Using GITM, *Yiğit and Ridley* [2011] have studied the variations of high-latitude Joule heating and auroral heating with increasing spatial resolution and the resulting effects on the ionosphere and thermosphere. *Yiğit and Ridley* [2011, Figure 7] present the Joule heating as a function of inverse latitudinal resolution at three representative altitudes, Q_J demonstrated an increase of >50% from the low to the high resolution case at around 500 km. A similar analysis in the current study shows that vertical winds demonstrate a peak increase of ∼15% in the lower thermosphere between the low and the high resolution, while the associated relative increase in the upper thermosphere is ∼8%. Also, the auroral heating increases ∼25% in the upper thermosphere (not shown).

4.2. High-Latitude Distributions of Vertical Winds

[21] Previous studies have suggested that high-latitude heat sources are possible mechanisms for the generation of strong upwelling events that can occur under disturbed geomagnetic conditions [*Rees et al.*, 1984; *Price et al.*, 1995]. In GITM, simulations with varying spatial resolution and quiet

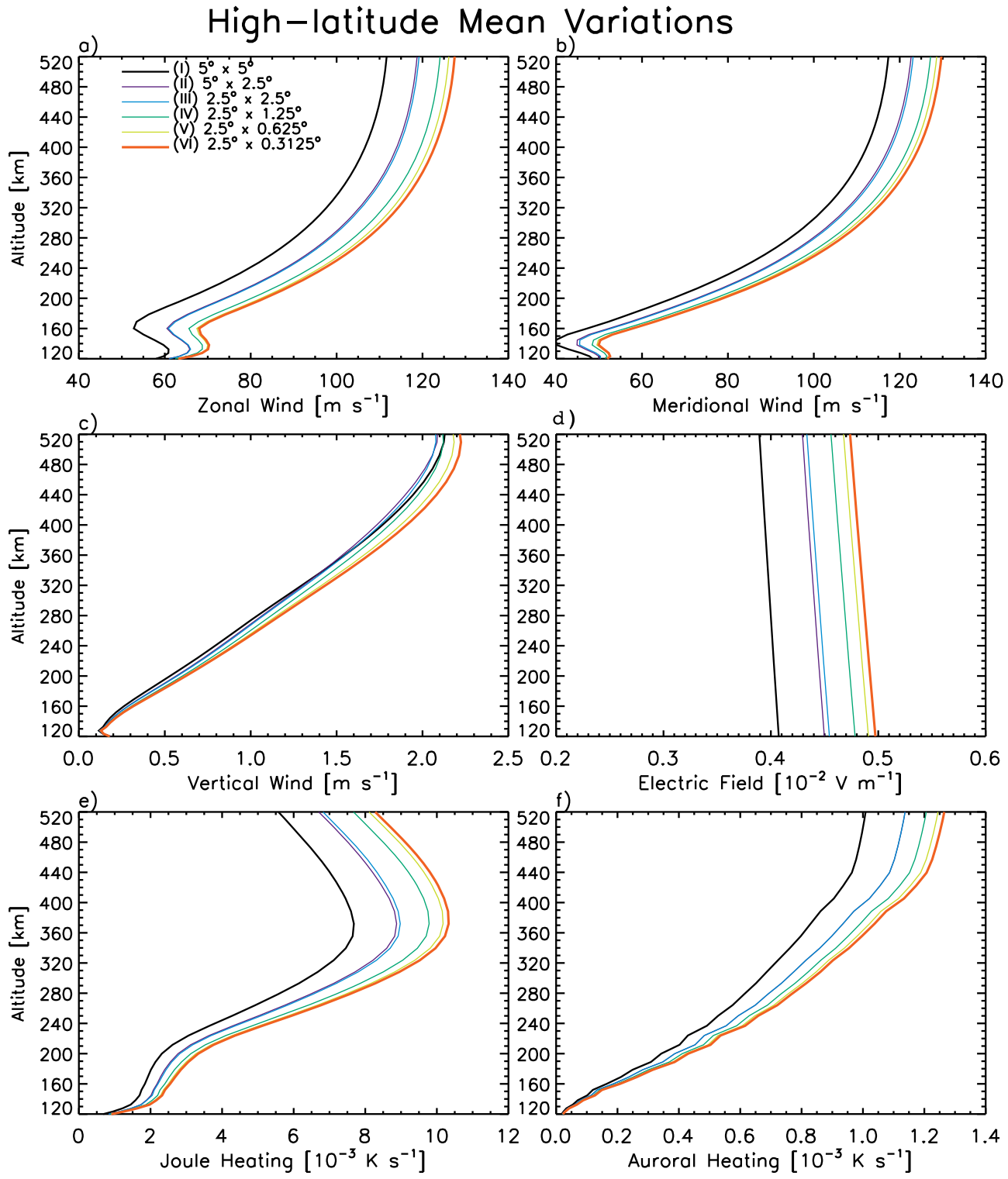

Figure 3. High-latitude mean thermosphere parameters simulated at increasing spatial resolution: (a) zonal, (b) meridional, and (c) vertical winds in m s^{-1}. (d–f) The associated results for electric field magnitude [V m^{-1}], Joule heating, and auroral heating, respectively, where the heating terms are in K s^{-1}. Area-weighted mean is calculated poleward of 50°N/S.

conditions have been assumed to explicitly focus on the effect of better resolving the thermosphere. It is of great interest to investigate possible correlations between the high-latitude heat sources and the vertical winds. Even satellite observations of vertical winds have relatively limited spatial resolution of ≥1° in latitude that may not capture small-scale variations [e.g., *Innis and Conde*, 2002]. Calibration of the absolute zero velocity reference and small vertical wind

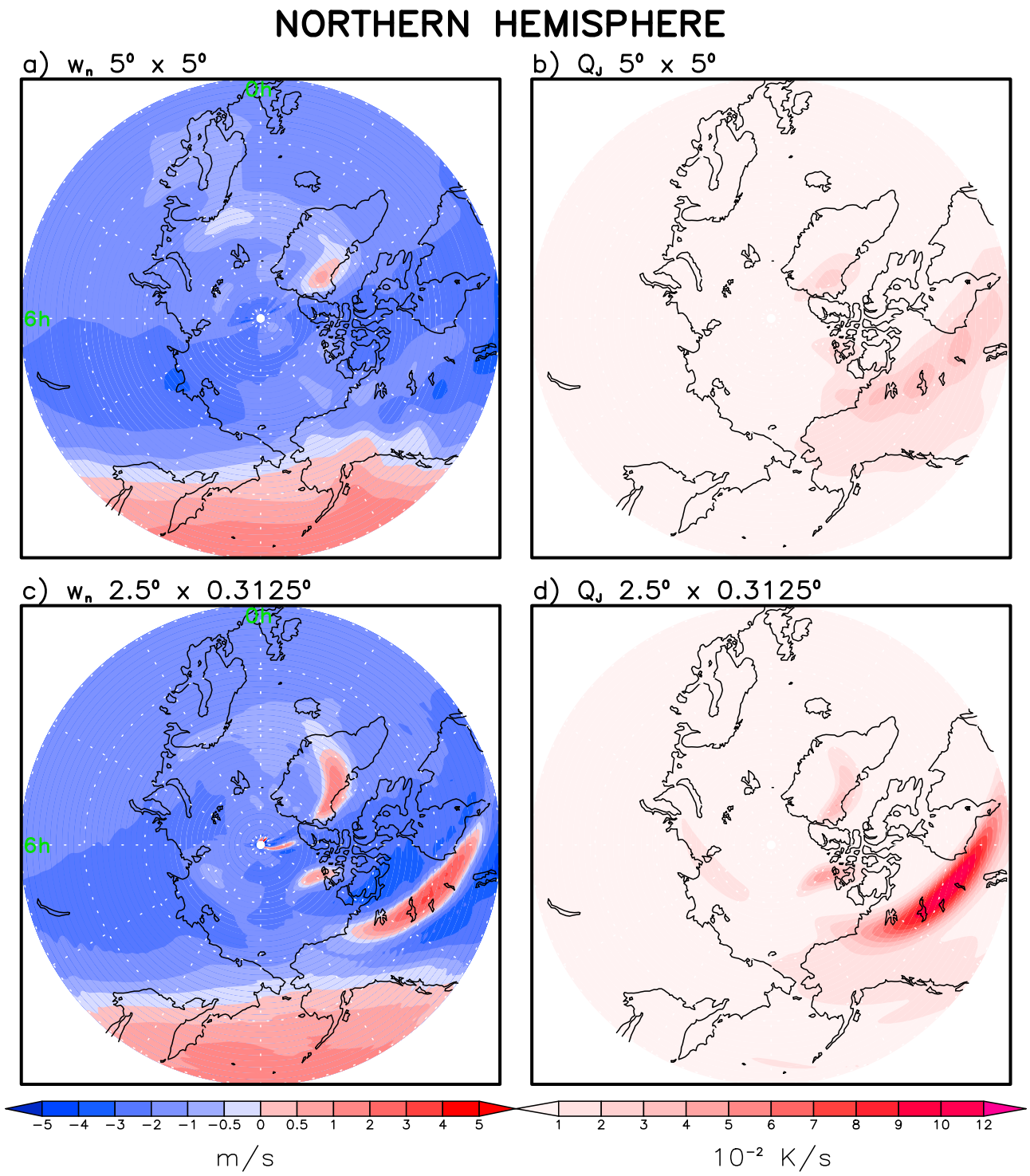

Figure 4. Northern Hemisphere (NH) high-latitude (poleward of ∼50°N) distributions of (a, c) vertical wind and (b, d) Joule heating at ∼375 km on 22 December 0000 UT. Representative model longitude-latitude resolutions are shown at 5° × 5° (Figures 4a and 4b) and 2.5° × 0.3125° (Figures 4c and 4d). Note that for reasons of visual simplicity, Joule heating has been scaled with 10^{-2} K s^{-1}.

amplitudes are challenging aspects of determining vertical winds unambiguously [*Conde and Dyson*, 1995]. Thus, models that enable very high latitudinal resolution are crucial to investigate the spatial details of the high-latitudes. For this, the high-latitude distribution of the Joule and auroral heat sources and the associated vertical winds at ∼370 km are plotted for the Northern Hemisphere (NH) in Figure 4. With increasing spatial resolution the Joule heating and vertical winds increase in magnitude. Large vertical winds are typically seen around noon time (12 h) at lower latitudes at all resolutions primarily as a consequence of solar illumination, but the lower resolution runs cannot capture the enhanced

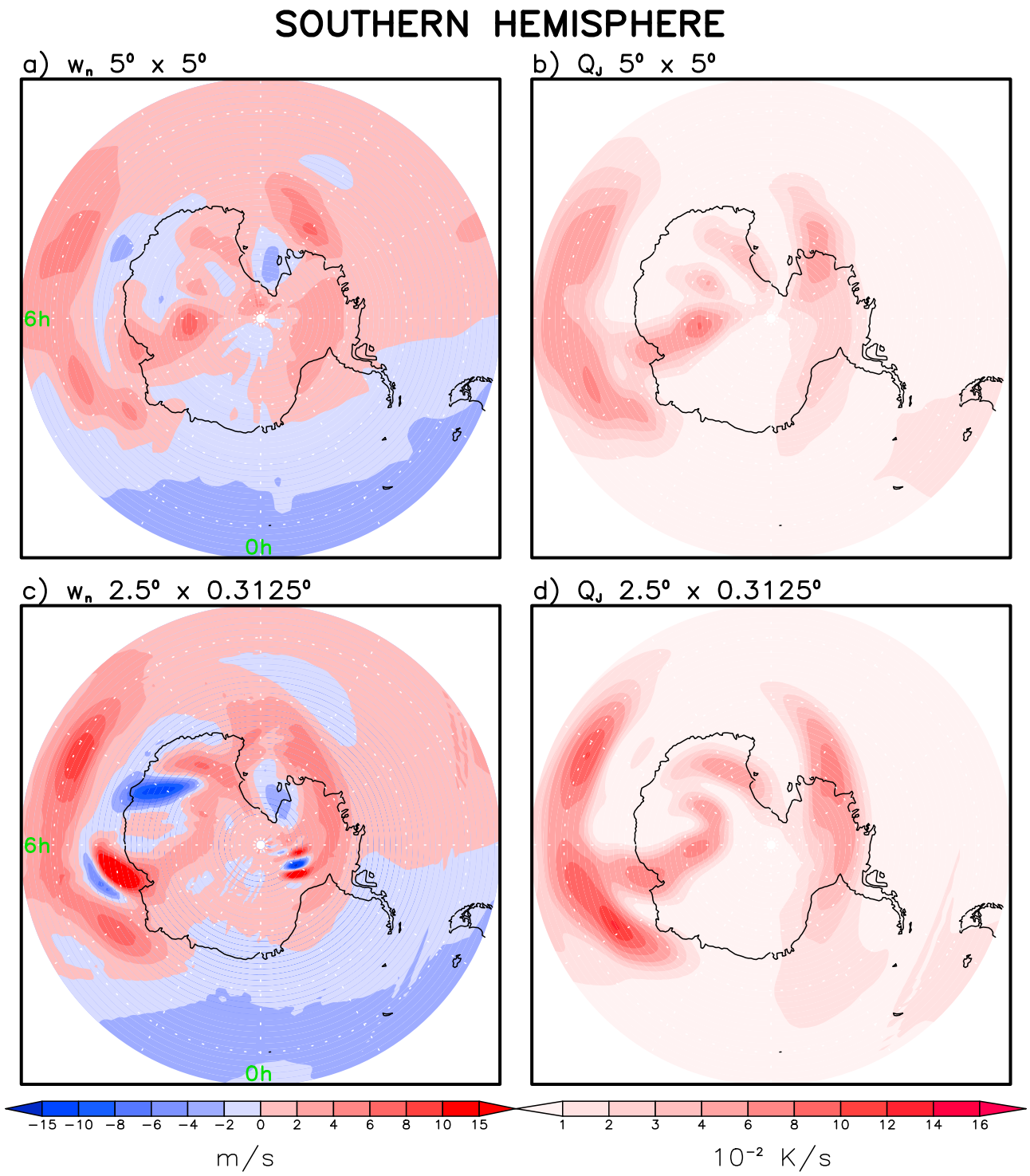

Figure 5. Same as Figure 4 but for the Southern Hemisphere (SH) high-latitudes.

vertical winds of up to 4 m s^{-1} that are simulated at the highest resolution near dusk at 60° latitude (Figure 4c). At the highest resolution these winds are as large as those seen at noon at low latitudes in the low resolution. This phenomenon is closely correlated to better resolved peak Joule heating at around 60°N situated in the noon-to-dusk sector (Figure 4d). Increasing the resolution (5° × 5° → 2.5° × 0.3125°) intensifies this localized Joule heating more than a factor of three, i.e., 3.5 → 12 × 10^{-2} K s^{-1}. This localized peak Joule heating is about 10 times larger than the heating rate that is typically associated with the solar UV in the thermosphere at this altitude and solar conditions.

[22] Figure 5 presents the associated results for the Southern Hemisphere, which is the summer hemisphere, in the same manner as Figure 4. Localized enhanced vertical winds are present at lower latitudes in the dawn sector and at higher latitudes around the dusk sector in the highest resolution (Figure 5c) that are only partially captured at the lower

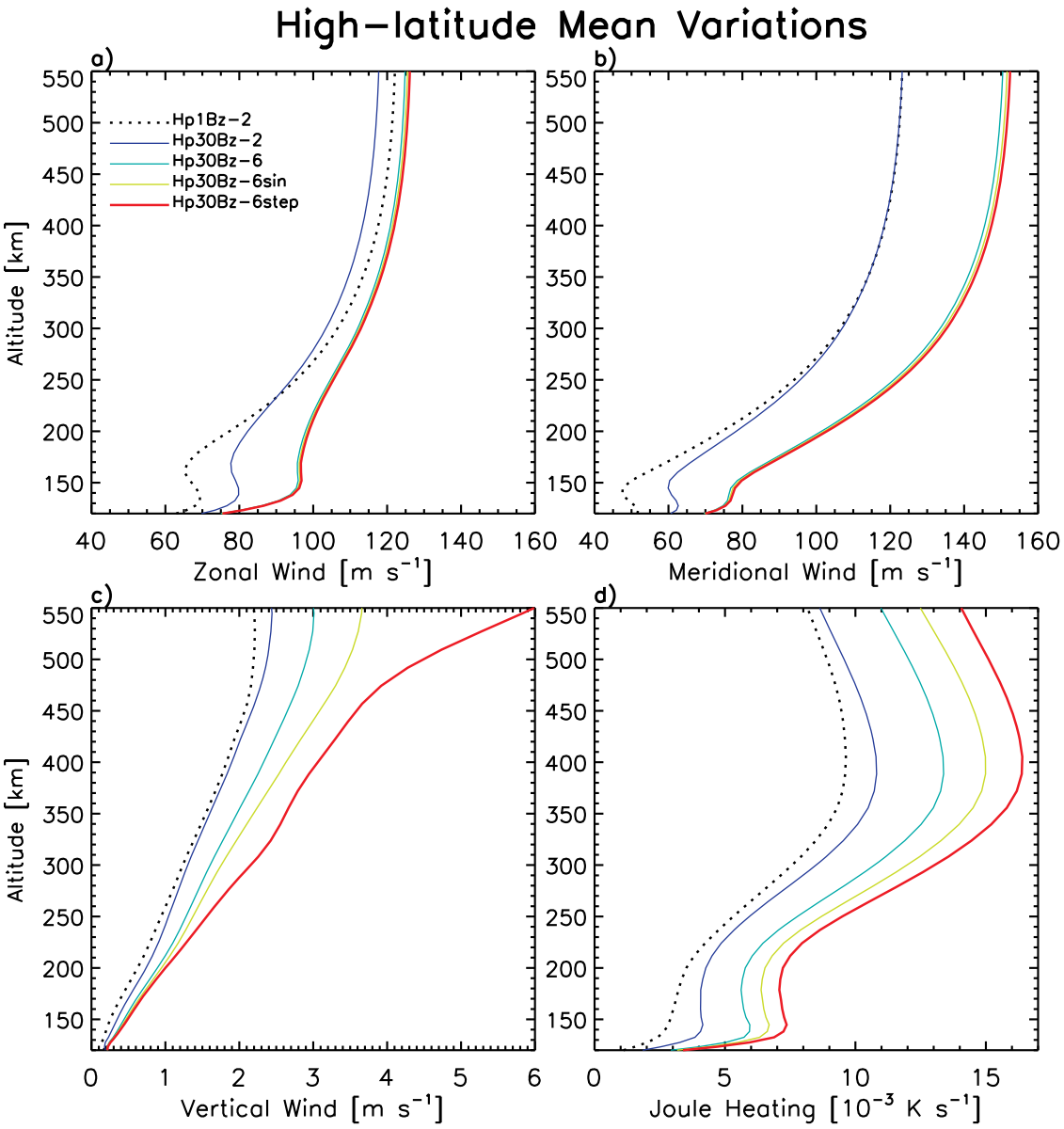

Figure 6. Southern and Northern Hemisphere combined high-latitude mean thermosphere parameters similar to Figure 3 but for different variations of IMF B_z and HP: (a) zonal, (b) meridional, and (c) vertical winds in m s^{-1} and (d) Joule heating (Q_J). Averaging has been performed for the period of 22 December 0000-0800 UT over outputs of 5 min. The different line colors represent the runs with the different configurations of IMF B_z and HP.

resolutions. In fact, the wave-like vertical wind structures manifested by vertical wind variations of ±20 m/s that are simulated around 80°S in the midnight to dusk sector are entirely absent in the 5° × 5° resolution. Discussion of the characteristics of these internal waves are beyond the scope of this paper.

5. Response of the Polar Ionosphere to Ion Flow Variability

[23] The following sections describe in detail the magnitude and temporal variability of the high-latitude neutral vertical winds under varying conditions of ion flows.

5.1. Global High-Latitude Mean Fields

[24] Figure 6 presents the high-latitude mean thermosphere parameters in a similar manner as in Figure 3 but for the period of 22 December 0000-0800 UT and for varying conditions of magnetospheric energy inputs as described in section 3.2 and illustrated in Figure 1. The different lines represent the different magnetospheric conditions described by IMF and HP variations. Note that the most quiescent condition (III_0), where B_z is kept constant at −2 nT, is denoted by black dotted lines. Increasing HP from 1 to 30 GW is seen to have a great impact on the auroral heating, increasing the mean magnitude from 1 to 6 × 10^{-3} K s^{-1} in the upper thermosphere (not shown), but a relatively small increase is seen in the peak Joule heating 9.5 → 11 × 10^{-3} K

s^{-1} (Figure 6d). The largest response of the vertical winds to increased auroral heating is seen in the upper thermosphere of about 0.2 m s^{-1} (2.2 to 2.4 m s^{-1}). Intensifying B_z has varying degrees of impact on the thermosphere parameters. A significant horizontal wind intensification is seen if $|B_z|$ is increased, with the upper atmospheric mean meridional winds demonstrating the largest increase. The vertical winds are affected remarkably, showing enhancements by the increased magnitude of the IMF and peaking at around 550 km with 6 m s^{-1} in the step-like ion flow variations.

5.2. High-Latitude Distribution of Vertical Winds in the Northern Hemisphere

[25] Figure 7 presents the polar stereographic distribution of NH vertical winds, Joule and auroral heating at ~370 km on 22 December at 0705 UT, plotted in an analogous manner as in Figure 4, but for varying conditions of magnetospheric inputs. This configuration gives an overview of how the distributions of w_n, Q_J, and Q_A vary with varying intensities of ion flows. Increasing HP from 1 GW to 30 GW (not shown) enhances the auroral heating by at least an order of magnitude, generating a spatially larger auroral oval, extending to lower latitudes and it is independent of ion flow variations. The main features of Figure 7 can be summarized as the following: (1) The B_z magnitude increase causes the Joule heating and vertical winds to increase; (2) Adding variability to ion flows causes both the Joule heating and vertical winds to increase dramatically; and (3) Vertical wind perturbations are observed to be appreciably larger in the step function run (III_{-6}^{step}) than in the sinusoidal variation run (III_{-6}^{sin}) although at this presented UT the instantaneous value of the cross polar cap potential (CPCP) in both runs are very similar (5% difference). For example, in the midnight to dawn sector the peak vertical winds are nearly a factor of 2 larger in the step function run than in the the sinusoidal case: ~8 versus ~16 m s^{-1}. Result 3 highlights an interesting feature of how the thermosphere-ionosphere system responds to varying ion flows. Close investigation of the vertical wind distribution along with the Joule heating suggests that sudden step-like variations in ion flows can lead to larger vertical winds than in the case of a sinusoidal variation, while similar Joule heating is produced. At this specific UT, the ion flows are similar to each other, but much larger vertical winds are produced in the case of the step function. In the following section, we investigate the details of the vertical wind enhancement seen in III_{-6}^{step} and possible mechanisms for it.

5.3. Temporal Variability of the High-Latitude Vertical Winds

[26] Temporal variations of some thermospheric parameters between 0100 and 0800 UT on 22 December at ~370 km for a representative location in the Northern Hemisphere high-latitudes (61.25°N, 37.25°W) are shown in Figure 8. The different line colors represents the different B_z runs with constant HP of 30 GW, but with varying IMF conditions, i.e., III_{30GW}, III_{-6}, III_{-6}^{sin}, and III_{-6}^{step}. The overall large-scale changes that are observed at this location are due to the rotation of the Earth through the sun-fixed ion flow patterns. Note that in the bottom row of Figure 7l, the green solid line at 61.25°N shows approximately how the longitude 37.25°W passes through the vertical wind, Joule heating, and auroral oval pattern as the Earth rotates through the seven hours shown (assuming that the patterns are roughly static). Overall, large rapid variations are seen in the horizontal motion of both ions and neutrals with increasing magnitude and degree of temporal variability of IMF B_z. Conversely, there is little variability observed in the electron density, which is a key element in controlling the Joule heating. After around 0400 UT time variations of the magnitude of all the three ion speeds u_i, v_i, and w_i, as well as Joule heating, and neutral vertical velocity increase rapidly. It is noteworthy that III_{-6}^{sin} and III_{-6}^{step} lead to similar variations in all parameters, except in w_n. The factor of two difference in the peak of w_n between III_{-6}^{sin} and III_{-6}^{step} at 0705 UT seen in Figure 7 appears to be a persistent feature extending over several UTs. The large variability seen in Joule heating in the different simulations must be controlled to a large extent by the imposed changes in ion flows in the different runs.

[27] In order to determine the possible relationship between the large vertical winds seen in III_{-6}^{step} and the horizonal flow, the temporal variability of the polar ionosphere is investigated. For this, the associated standard deviations ($\bar{\sigma}$) of the ion and neutral flows are studied from 0400 to 0600 UT, based on the 5-min model outputs, for each model spatial grid point.

[28] Figure 9 shows the Northern Hemisphere polar stereographic distribution of mean horizontal ion flow vectors and its standard deviation $\bar{\sigma}_{\mathbf{u}_{i_H}}$ (Figures 9a–9c) and the mean horizontal neutral flow vectors and the standard deviation of neutral vertical winds $\bar{\sigma}_{w_n}$ (Figures 9d–9f) at ~370 km. All units are in m s^{-1} and plots are poleward of 60°N. Ions flows are much faster than the neutrals due primarily to high-latitude momentum deposition. Regions of enhanced mean horizontal ion flow show large mean standard deviations, demonstrating a significant increase from III_{-6} to III_{-6}^{step} with peak $\bar{\sigma}$ of more than 300 m s^{-1} in the latter case. Comparable relatively large convection velocities were observed at high-latitudes by *Bristow* [2008]. The structure of the standard deviations though remains very similar. The mean neutral flow is much slower than the ion flow. However, it is striking that the vertical wind variability expressed by its standard deviations $\bar{\sigma}_{w_n}$, increases in the same manner as in the case of the standard deviations of the ion flows from III_{-6} to III_{-6}^{step}, that is, with more rapidly varying B_z conditions (from left to right). For example, in the III_{-6}^{step} run in the region east of Greenland and west of Iceland, $\bar{\sigma}_{w_n}$ exceeds 6.5 m s^{-1}, increasing nearly by a factor of two with respect to III_{-6}^{sin} in the same region. Comparison of $\bar{\sigma}_{\mathbf{u}_{i_H}}$ with $\bar{\sigma}_{w_n}$ indicates a distinct correlation between the variability of the ion flow and the vertical neutral motion.

[29] Figure 10 presents the associated results for the Southern Hemisphere poleward of 60°S. Similar to the case of the Northern Hemisphere, horizontal ion flows and their standard deviations and as well as the vertical wind variability are enhanced and demonstrates appreciable structural correlation in their distributions. Again, $\bar{\sigma}_{w_n}$ peaks in run III_{-6}^{step} with much larger values than Northern Hemisphere: >30 m s^{-1} versus >6.5 m s^{-1}, primarily owing to differences in the solar irradiation and Joule heating between the different hemispheres.

[30] Additionally, comparison of the results for $\bar{\sigma}_{w_n}$ in both hemispheres suggests that the relative increase/variation in

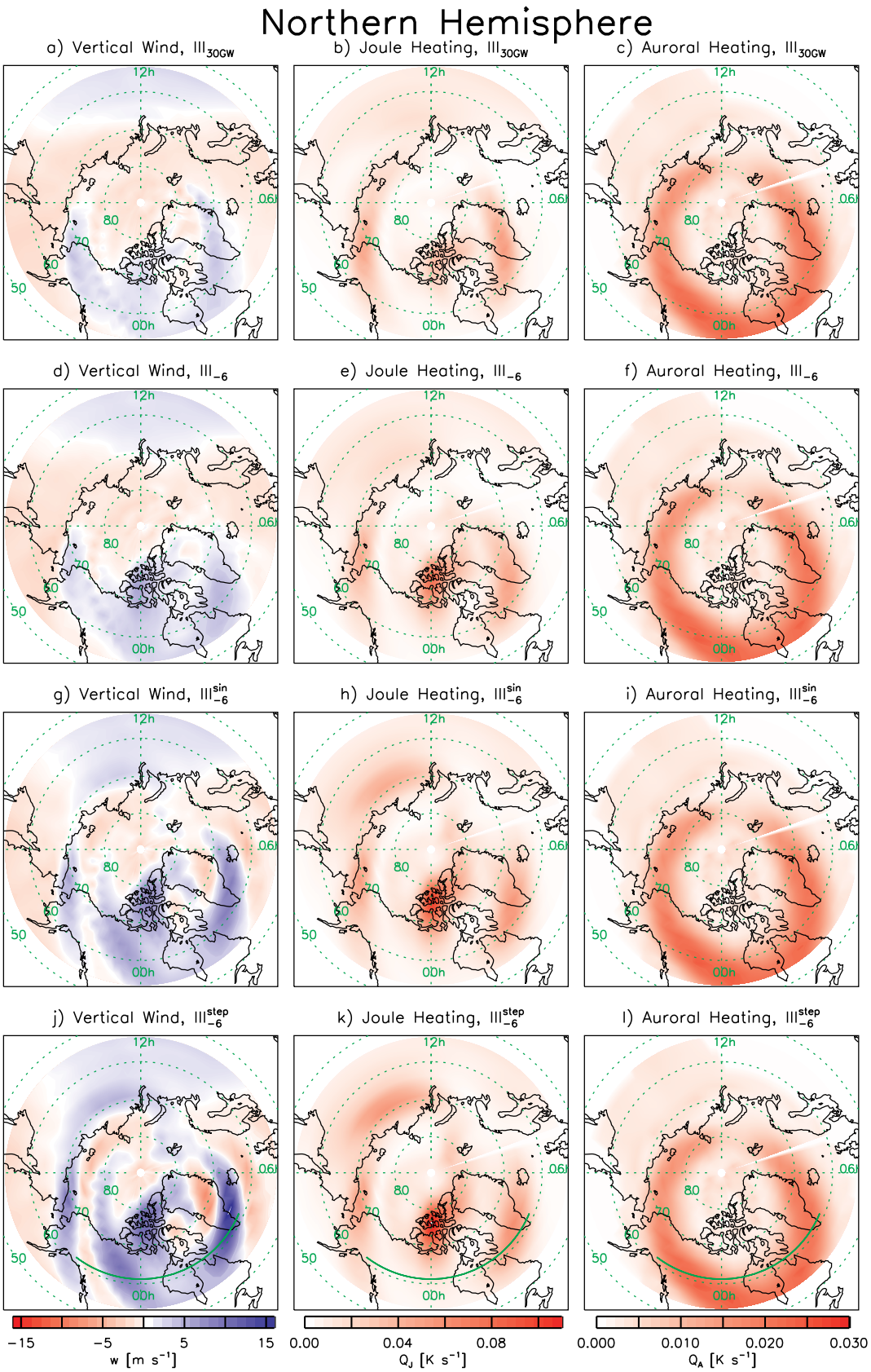

Figure 7. Northern Hemisphere (NH) high-latitude (poleward of ∼53.5°N) distribution of (a, d, g, j) vertical wind, (b, e, h, k) Joule heating, and (c, f, i, l) auroral heating at ∼375 km on 22 December 0705 UT. Shown are runs of varying magnetospheric conditions: III_{30GW} (Figures 7a–7c), III_{-6} (Figures 7d–7f), III_{-6}^{sin} (Figures 7g–7i), and III_{-6}^{step} (Figures 7j–7l). See the text for further details.

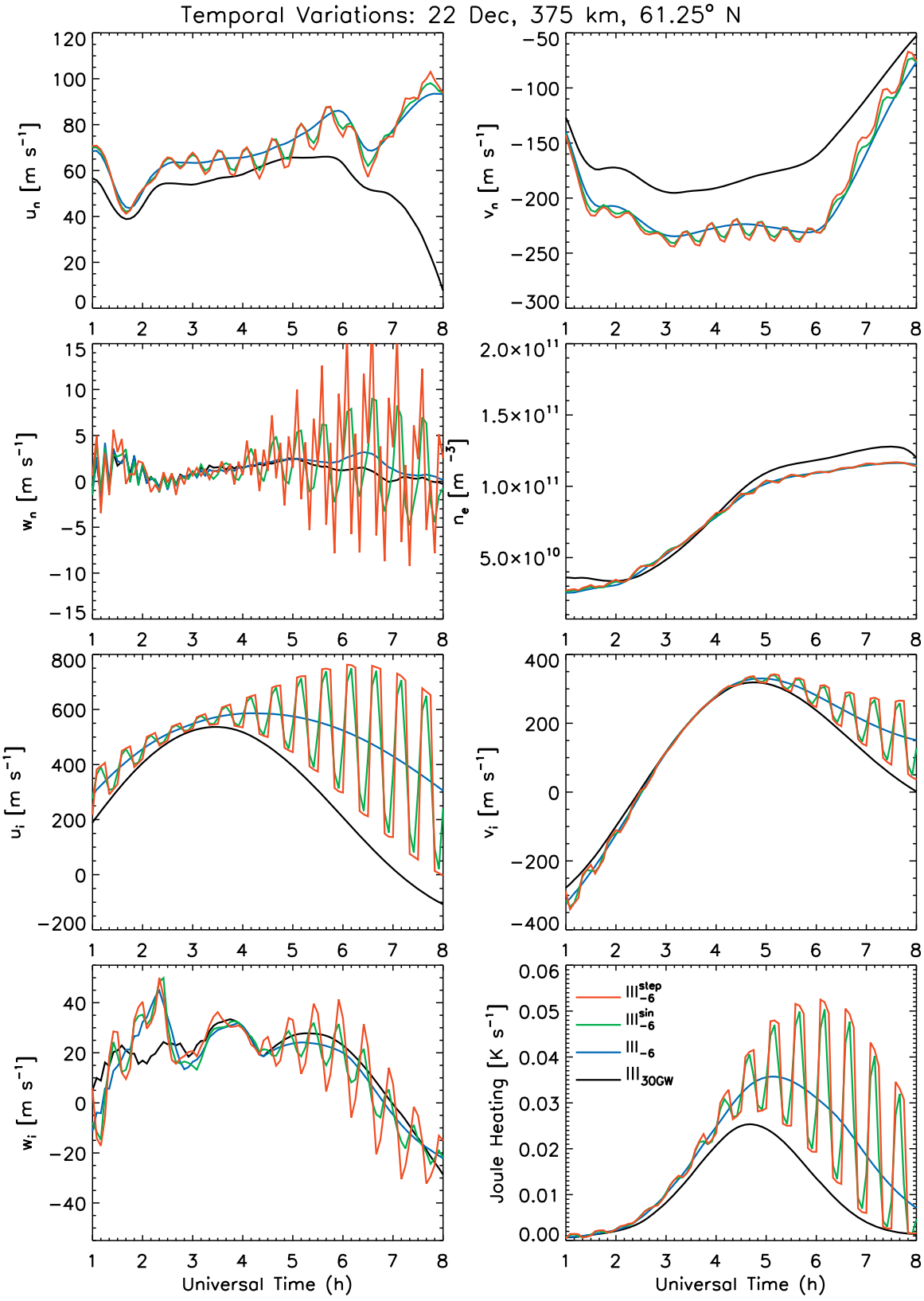

Figure 8. Temporal variation of the vertical wind along with other model parameters at ~375 km in Northern Hemisphere (61.25°N, 37.25°W). The different colors represent the different simulations with varying magnetospheric conditions: III_{30GW} (black), III_{-6} (blue), III^{sin}_{-6} (green), and III^{step}_{-6} (red). See the text for further details.

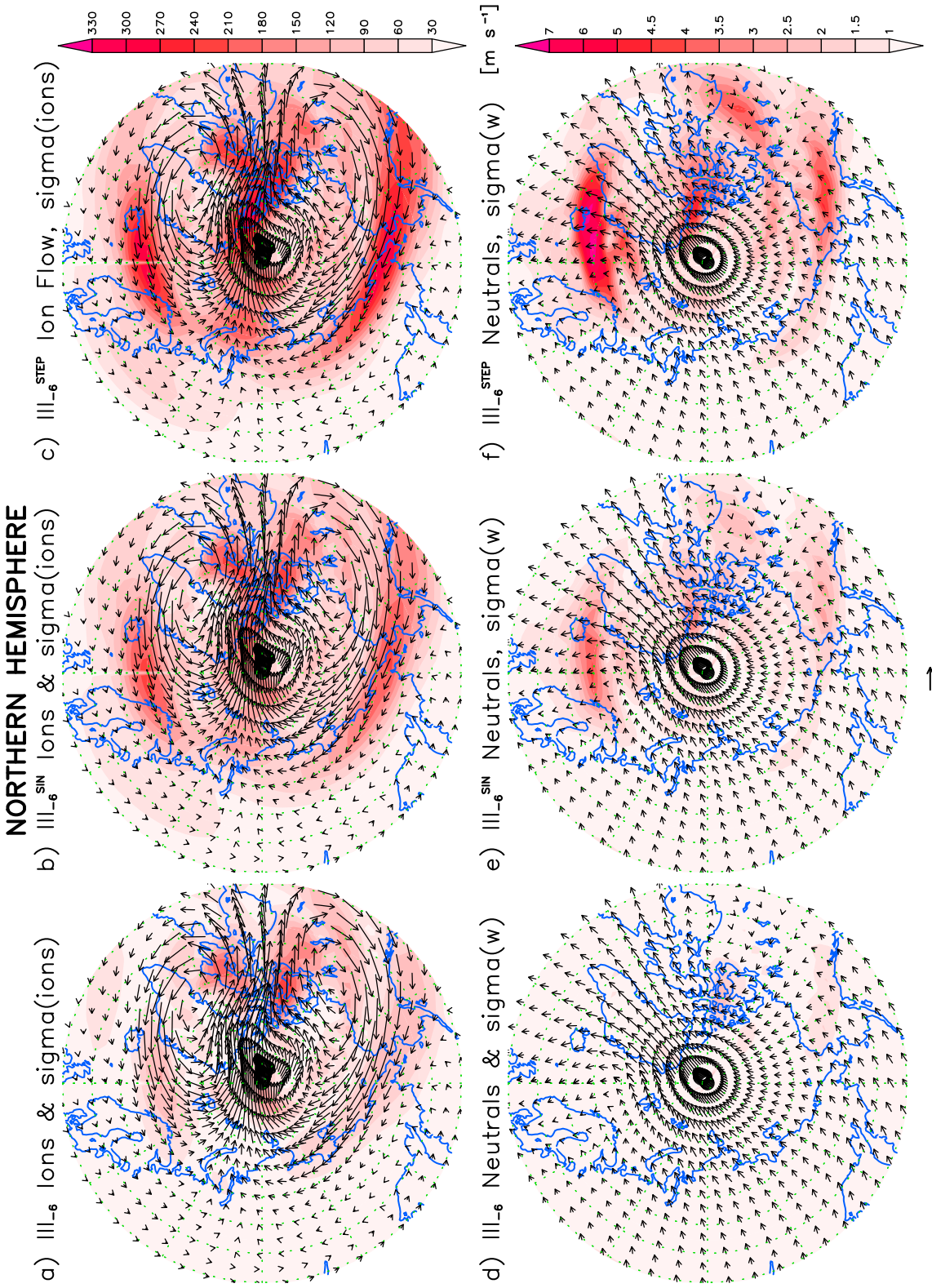

Figure 9. Northern Hemisphere results poleward of 55°N at ~375 km: III_{-6}, III_{-6}^{sin}, and III_{-6}^{step}. Shown are (a–c) the ion flow standard deviation in color shading, with the mean ion flow is overplotted with black vectors, and (d–f) the vertical neutral wind standard deviation in color shading along with the mean neutral flow in vectors. All units are in m s^{-1}. Universal times from 0400 till 0600 are considered.

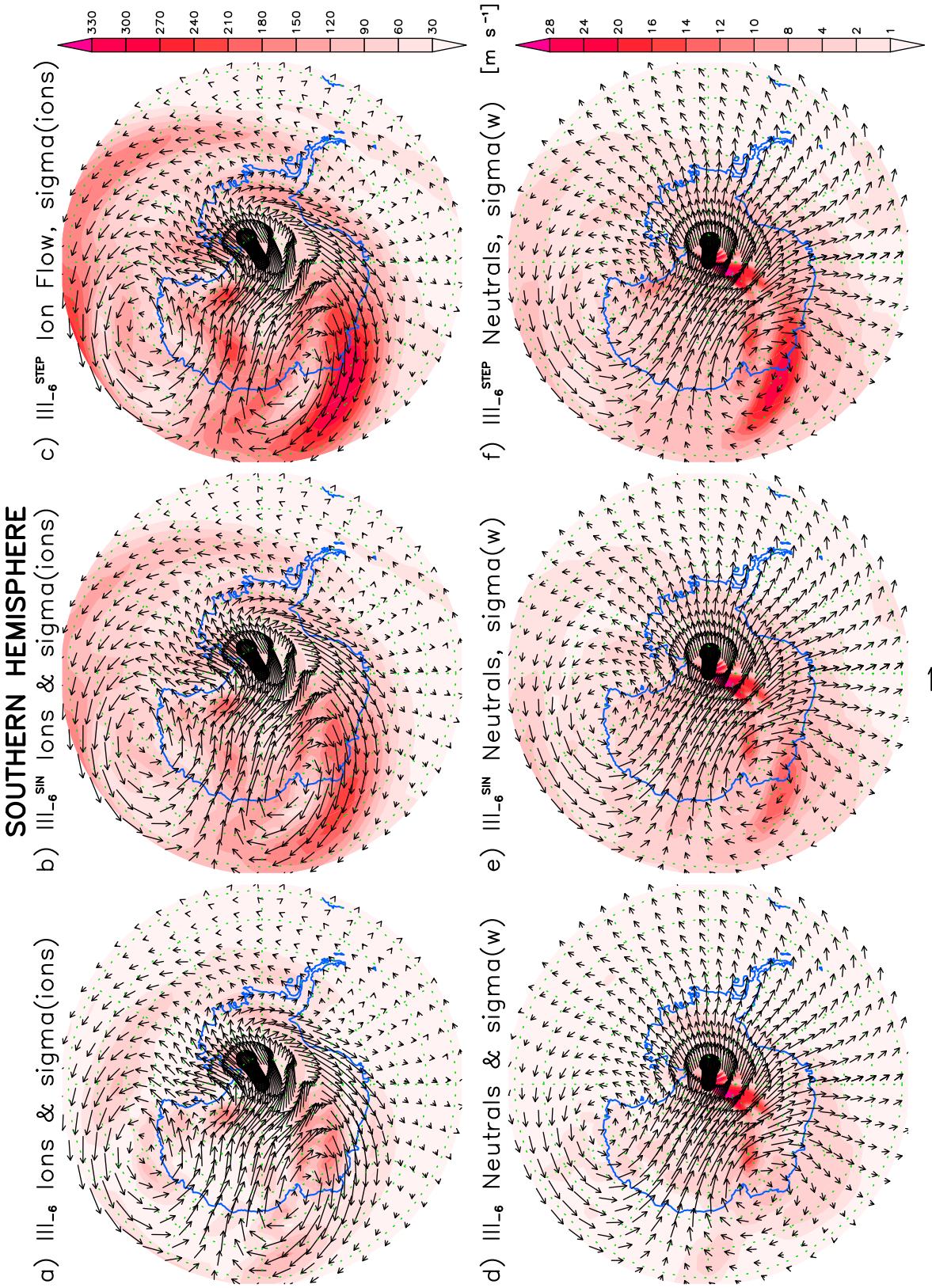

Figure 10. Same as Figure 9 but for the Southern Hemisphere poleward of 55°S.

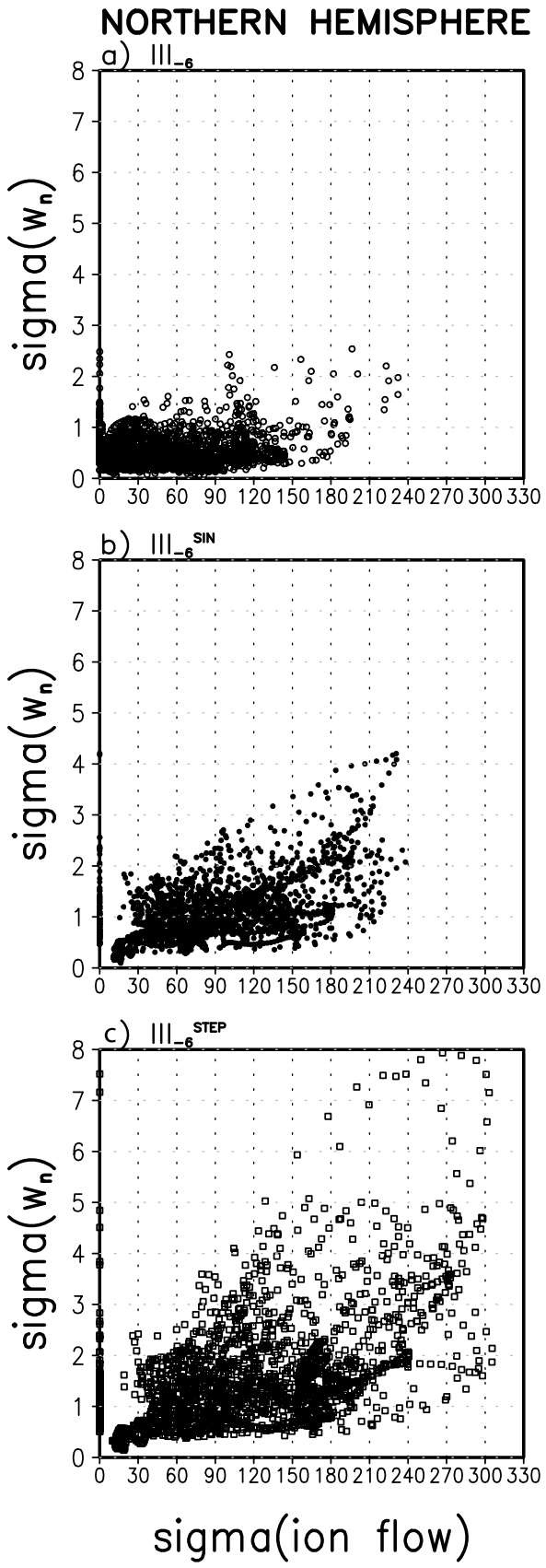

Figure 11. Scatterplots of $\bar{\sigma}_{w_n}$ versus $\bar{\sigma}_{\mathbf{u}_{i\perp}}$ for the Northern Hemisphere high-latitudes presented in Figure 9: (a) III_{-6}, (b) III_{-6}^{sin}, and (c) III_{-6}^{step}.

$\bar{\sigma}_{w_n}$ between the different runs are much larger (percentage-wise) in the Northern than in the Southern Hemisphere, demonstrating an asymmetry in the way the different hemispheres respond to temporal variations of the ion flows.

[31] Figure 11 shows how the vertical wind variability ($\bar{\sigma}_{w_n}$) presented in Figure 9 varies as a function of ion flow variability ($\bar{\sigma}_{\mathbf{u}_{i\perp}}$) in the Northern Hemisphere high-latitudes during the studied time interval (0400-0600 UT) for the cases of static, fast, and sudden ion flow changes. An increasing linear slope is seen between $\bar{\sigma}_{w_n}$ and $\bar{\sigma}_{\mathbf{u}_{i\perp}}$ as the characteristics of the perturbations become sharper. In the Southern summer high-latitudes (shown in Figure 12), where radiative processes play an important role besides plasma dynamics, variability of ion flows plays a similar significant role in producing large $\bar{\sigma}_{w_n}$. In this case, though, the slope does not appear to change as dramatically as in the winter hemisphere. More variability in the ion flows leads to more variability in the vertical winds, but the slope of that relationship may be solar illumination dependent and depends thus on the characteristics of the change perhaps.

[32] Relatively large $\bar{\sigma}_{w_n}$ values in Figure 12 that coincide with $\bar{\sigma}_{\mathbf{u}_{i\perp}}$ of $\sim$40 m s^{-1} are suggestive of possible small-scale wave processes that are capable of perturbing the vertical wind fields. These occur poleward of 80°S and maybe physical or numerical, since they are so close to the pole. It is unclear at this time what is causing this extremely high latitude structure.

[33] Altitude profiles of the standard deviations of neutral vertical winds and the ion horizontal flow at 65°S and 60°E illustrate to what extent, in terms of vertical depth, the ion flow shapes the vertical wind variability (Figure 13). Peak $\bar{\sigma}_{w_n}$ and $\bar{\sigma}_{\mathbf{u}_{i\perp}}$ occur in the upper thermosphere, with increasing peak magnitudes from III_{-6} to III_{-6}^{step}: $\sim$2 m s^{-1}, $\sim$25 m s^{-1}, and >40 m s^{-1} for III_{-6}, III_{-6}^{sin}, and III_{-6}^{step} at 550 km, respectively. With intensifying conditions of magnetospheric variability ($III_0 \rightarrow III_{-6}^{step}$), $\bar{\sigma}_{w_n}$ enhances rapidly with increasing altitude, producing overall increasing relative difference in $\bar{\sigma}_{w_n}$ between the different simulations. Although III_{-6}^{sin} and III_{-6}^{step} have similar $\bar{\sigma}_{w_n}$ in the lower thermosphere at $\sim$150 km, their magnitudes are nearly a factor of 2 larger than the constant magnetosphere simulation (III_{-6}): 2 versus 4 m s^{-1}. Also, $\bar{\sigma}_{\mathbf{u}_{i\perp}}$ increases dramatically with varying conditions of ion flows, but the profiles remain relatively constant with altitude. These results support the finding that overall the imposed ion flow variabilities greatly impact the vertical wind variability in the upper thermosphere, while nonnegligible impact is still seen in the lower thermosphere down to 150 km.

[34] Finally, Figure 14 presents the vertical variation of w_n from 0400-0600 UT at 65°S and 60°E for static (Figure 14a), fast (sinusoidal, Figure 14b), and suddenly changing (step, Figure 14c) ion flows. Vertical neutral winds are upwards everywhere in the static ion flow simulation with increasing magnitude from the lower to the upper thermosphere and peaking at around 550 km with >16 m s^{-1}. This agrees with Figure 7, which shows a large region of strong upward flow in the auroral oval region. In the fast varying ion flows, vertical winds alternate the direction about every 15 min in accordance with the imposed ion flow changes. Peak upward and downward winds are >40 m s^{-1} and <−8 m s^{-1}. In the step-like ion flow variations (Figure 14c), the w_n variations reach ±40 m s^{-1} in the upper thermosphere with a distinct

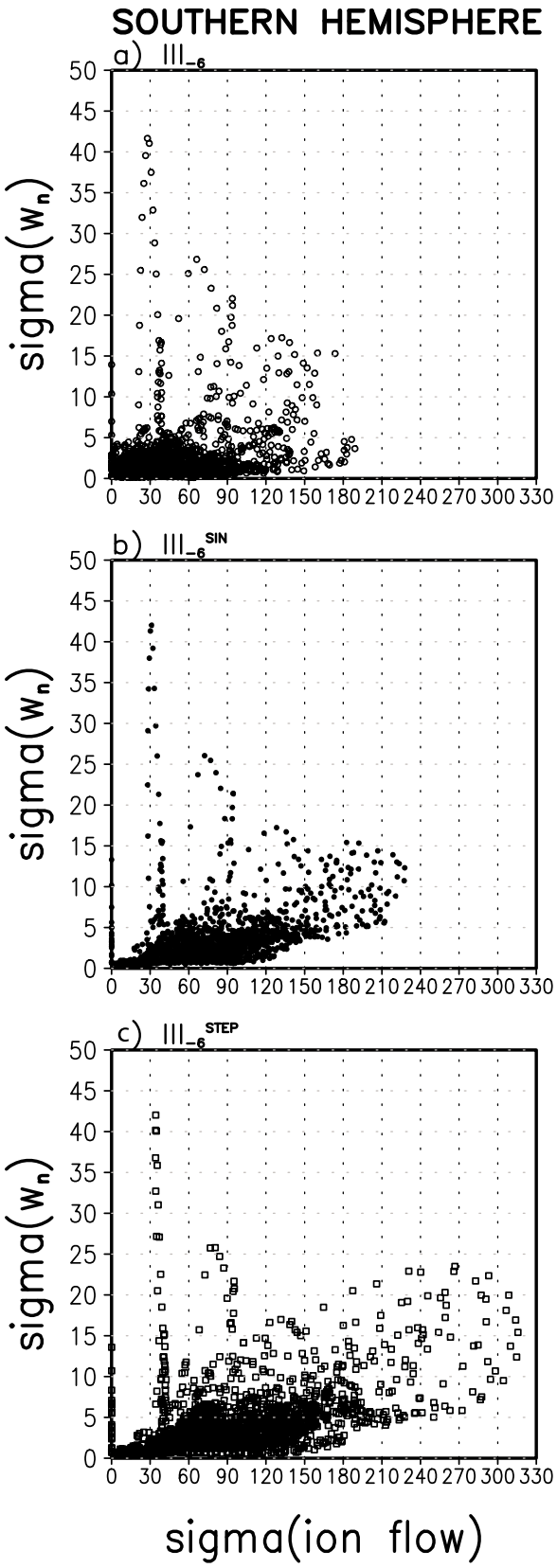

Figure 12. Scatterplots of $\bar{\sigma}_{w_n}$ versus $\bar{\sigma}_{\mathbf{u}_{in}}$ for the Southern Hemisphere high-latitudes presented in Figure 10: (a) III$_{-6}$, (b) III$_{-6}^{\sin}$, and (c) III$_{-6}^{step}$.

tilted phase front suggestive of vertically propagating internal waves. It is evident from the presented suit of model simulations that ion flow variations are potentially capable of impacting magnitude, direction, and temporal variability of neutral vertical winds in the thermosphere.

5.4. Investigation of Mechanisms Controlling Vertical Winds

[35] The modeling results so far demonstrate a remarkable relationship between the plasma flow variability and the neutral thermospheric vertical winds. In order to gain further insight into the possible mechanisms of how plasma flows

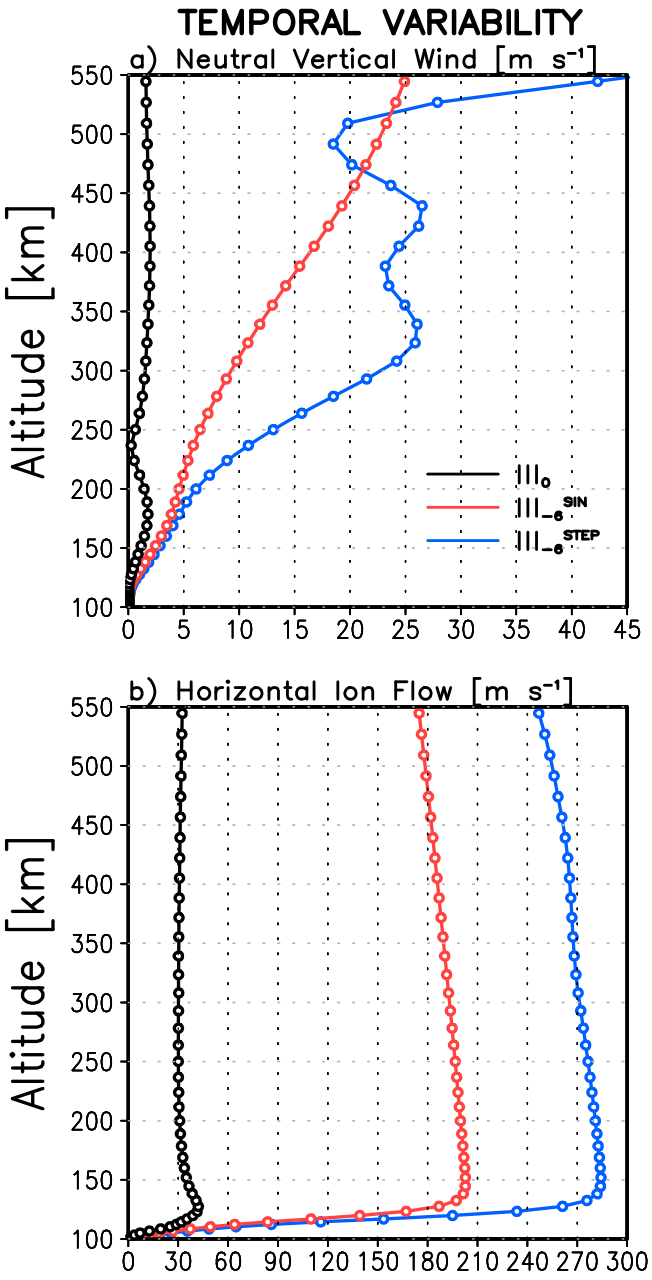

Figure 13. Vertical profiles of the temporal variability ($\bar{\sigma}$) of (a) vertical neutral winds and (b) horizontal ion flow in the Southern Hemisphere at 65°S and 60°E. Black, red, and blue curves represent III$_{-6}$, III$_{-6}^{\sin}$, and III$_{-6}^{step}$, respectively.

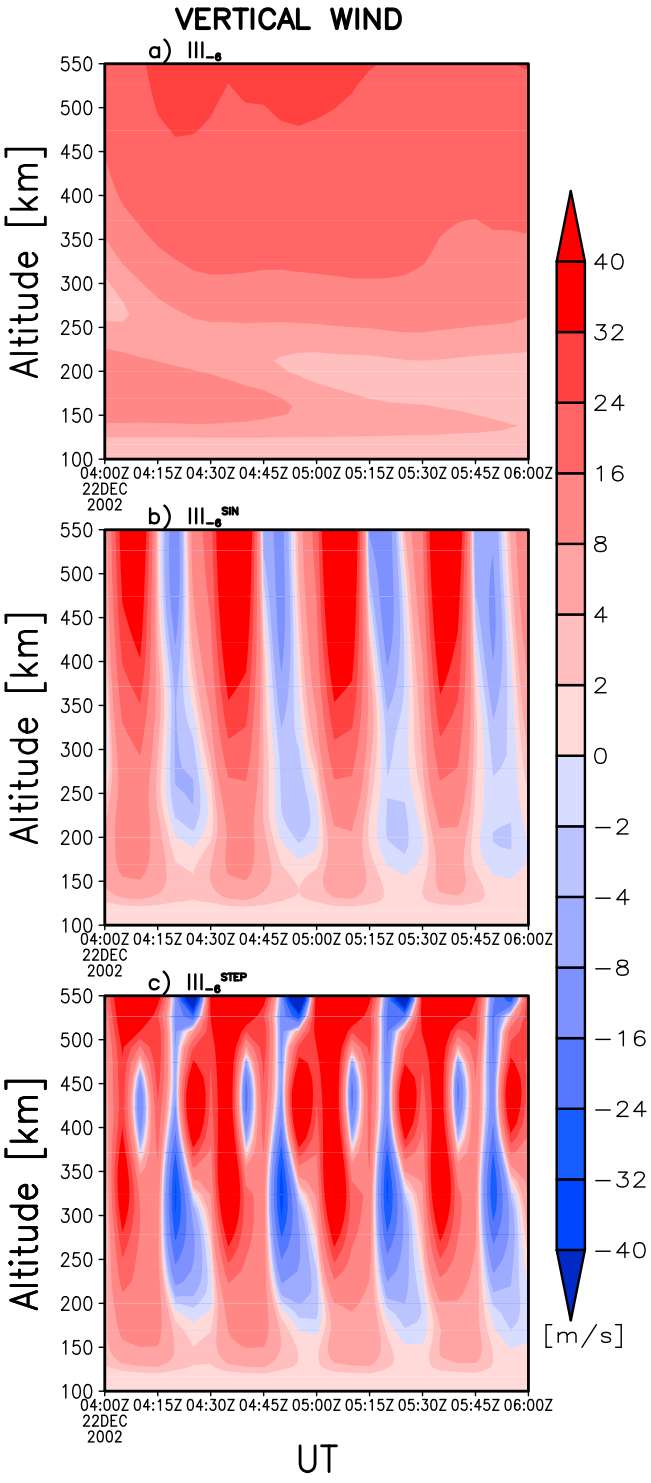

Figure 14. Altitude-UT cross sections of vertical winds in the Southern Hemisphere at 65°S and 60°E for (a) III_{-6}, (b) III_{-6}^{sin}, and (c) III_{-6}^{step}.

can impact the vertical winds, first the vertical acceleration is examined from 0400 to 0500 UT in a representative winter Northern Hemisphere high-latitude (68.75°N, 180° longitude) at ~400 km. Figure 15 presents the UT variations of vertical acceleration ($a \equiv \partial w_n/\partial t$) (Figure 15a), vertical wind (w_n) (Figure 15b), temperature (Figure 15c), Joule heating (Figure 15d), and divergence of the horizontal neutral winds, $\nabla \cdot \mathbf{u}_{n_H}$ (Figure 15e). In Figure 15a, the subscripts "nhyd", "sph", "in", "nn", and "cor" denote the vertical acceleration in m s^{-2} due to nonhydrostatic effects (that is, imbalance between thermal expansion and the gravitational force), spherical geometry (sphericity), vertical ion drag, neutral friction, and coriolis plus centrifugal effects. Accordingly, equation (2) can be expanded further in spherical coordinates as [*Ridley et al.* 2006, Equation 14]

$$\frac{\partial w_n}{\partial t} + w_n \frac{\partial w_n}{\partial r} + \frac{v_n}{r}\frac{\partial w_n}{\partial \theta} + \frac{u_n}{r\cos\theta}\frac{\partial w_n}{\partial \theta} = -\frac{k_b}{m_s}\frac{\partial T}{\partial r} - \frac{k_b T}{m_s n_s}\frac{\partial n_s}{\partial r} + g + \frac{u_n^2 + v_n^2}{r} + a_{in} + a_{nn} + a_{cor}, \quad (3)$$

where θ is latitude, k_b is the Boltzmann constant, n_s and m_s are the number density and molecular mass of a species s, respectively.

[36] In our calculations, the nonhydrostatic acceleration is given by superposing the upward directed pressure force on the downward directed gravitational acceleration. So, effectively, positive $w_{t,nhyd}$ will drive upward vertical winds, while negative $w_{t,nhyd}$ will drive downward vertical winds, depending on the contributions from other possible physical mechanisms.

[37] In Figure 15a, it is seen that the nonhydrostatic acceleration varies dramatically with variable plasma flows, peaking in the case of rapidly varying plasma flows. The accelerations due to other sources (vertical ion drag, etc.) appear to be unaffected by plasma flow variations. The resulting neutral vertical winds are shown in Figure 15b. Temporal variations of the vertical winds resemble closely the static (const), sinusoidally varying (sin), and step-like varying (step) plasma flows. The highest vertical wind magnitudes and variability are seen in the simulation with the sudden plasma flow variations (III_{-6}^{step}). The associated extrema in w_n follow closely the nonhydrostatic acceleration, which implies that with increasing intensity of plasma flow variations, nonhydrostasy becomes the dominant physical mechanism that controls the magnitude and variation of neutral vertical winds.

[38] The next step is the question of what can cause enhanced nonhydrostasy. For this, neutral temperature, neutral gas heating by frictional heating (Joule heating), and horizontal neutral wind divergence are investigated for the same period of universal time (Figures 15c–15e). Overall, the temperature variations demonstrate some degree of similarity to w_n. The rapid plasma flow variation case shows the largest temperature variations and detailed investigation suggests that temperature extrema are typically preceding the w_n extrema. Joule heating is seen to resemble exactly the behavior of plasma flow variations with 15-minute variations in slowly and rapidly varying plasma flow simulations. The static case has relatively constant Joule heating within the shown 60 min. Examining Joule heating along with the temperature and vertical winds highlights an interesting phenomenon of thermosphere-ionosphere coupling. Plasma flows can enhance Joule heating due to larger differential motion between the ions and neutrals [e.g., *Yiğit and Ridley* 2011, equation 2]. This heats up the atmosphere and

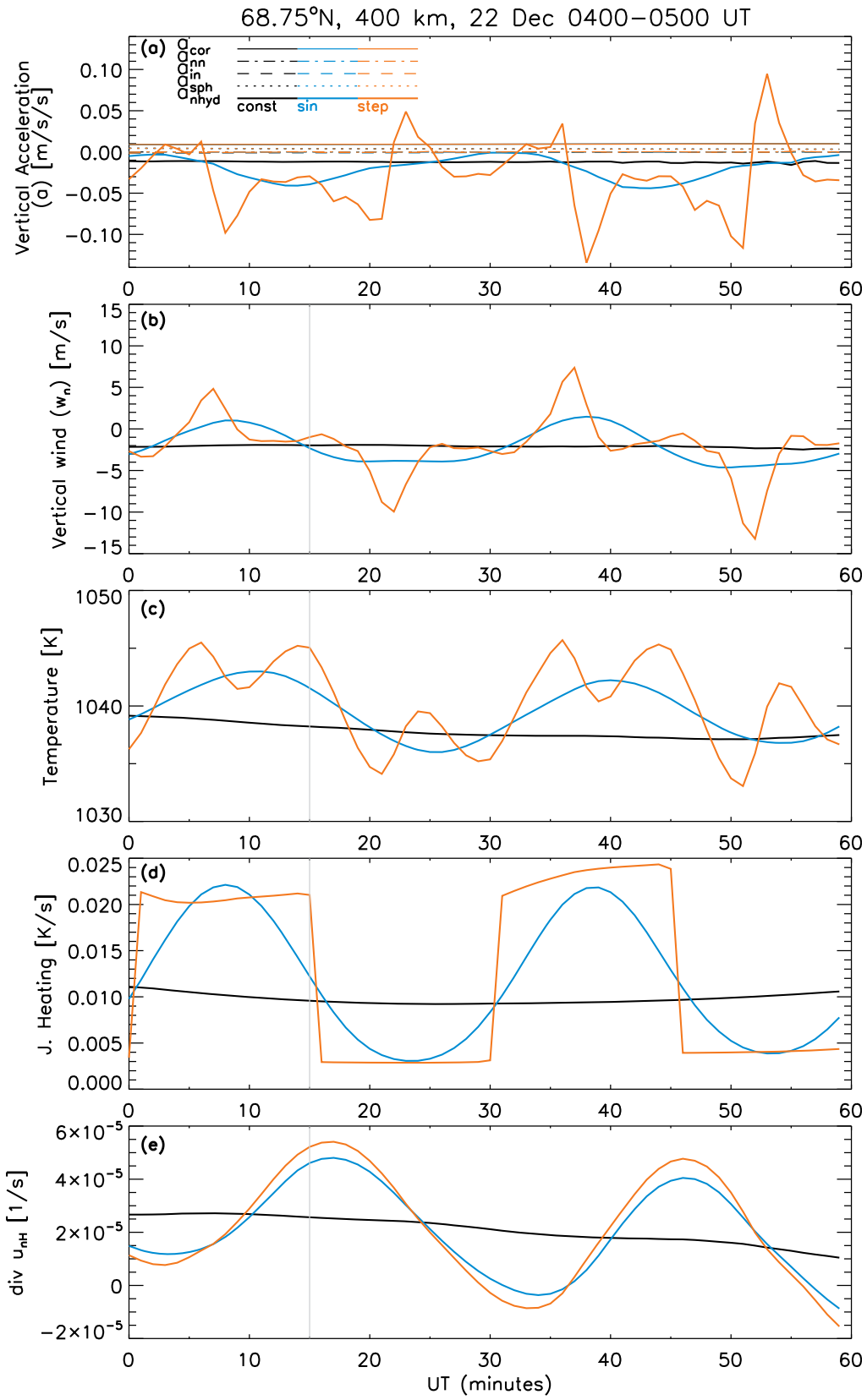

Figure 15. Universal time variations of (a) vertical acceleration ($a \equiv \partial w_n/\partial t$), (b) vertical winds ($w_n$), (c) temperature, (d) Joule heating, and (e) divergence of the horizontal neutral winds for a representative high-latitude location (68.75°N and 180° longitude) in the winter Northern Hemisphere for the static (III_{-6}, black), slowly varying (III_{-6}^{sin}, blue), and rapidly varying plasma flow (III_{-6}^{step}, yellow) simulations on 22 December between 0400 and 0500 UT.

generates localized upward vertical winds (upwelling) and results in enhanced horizontal divergent flow [*Smith*, 1998]. In turn, upwelling can adiabatically cool the atmosphere producing the local temperature minima seen after temperature maxima in the step-like variation simulation. Local horizontal divergence demonstrates a remarkable correlation with the Joule heating, showing maximum increase in divergence when Joule heating is enhanced by rapidly varying ion flows (III_{-6}^{step}), although this is quite smooth, unlike the vertical winds.

[39] Gravitational acceleration is not affected by plasma flow variations, thus the only way an enhanced imbalance between the pressure force and gravity can occur is via variations in the pressure gradient. This can occur via changes in the vertical gradient of temperature, $T_r \equiv \partial T/\partial r$, and/or in the vertical gradient of number density, $n_r \equiv \partial n/\partial r$ (see Appendix A). Changes in horizontal divergence can affect both quantities, T_r via the thermodynamic energy equation and n_r via continuity. In GITM, the continuity equation for a species n_s

$$\frac{\partial n_s}{\partial t} = -n_s(\nabla\cdot\mathbf{u_n}) - \mathbf{u_n}\cdot\nabla n_s \tag{4}$$

is expressed in spherical polar coordinates as horizontal and vertical continuity equations [*Ridley et al.*, 2006, equations 12 and 18]. Variations of horizontal divergence between the three simulations can lead to different vertical gradients of T and n. This effect is additionally enhanced by vertically varying Joule heating, which can have different vertical profiles in the different simulations as can be seen in Figure 6, indicating that static, slowly varying, and rapidly varying plasma flows will certainly impact Joule heating differently at different altitudes, generating variations in horizontal divergence and thus in T_r and n_r between the different simulations and hence different degrees of nonhydrostasy.

[40] From the analysis shown in Figure 15, it appears that the differential heating as a function of altitude when the Joule heating is changed suddenly causes an imbalance in the hydrostatic conditions, leading to strong vertical flows. While the divergence of the horizontal winds does have an effect on the vertical winds, it is a slow process that is unable to respond to the more rapid variations in the heating.

6. Discussion and Conclusions

[41] Using the University of Michigan Global Ionosphere Thermosphere Model (GITM), the impact of model temporal and spatial variability on the magnitude and distribution of the high-latitude vertical winds have been investigated. First a set of six simulations of increasing spatial resolution from 5° × 5° to 2.5° × 0.3125° have been performed at low geomagnetic and moderate solar activity. To investigate the impact of temporal variability, magnetospheric input has been modulated in a number of systematic simulations, using various forms of UT variations of the vertical component of the interplanetary magnetic field (IMF), B_z, such as constant, sinusoidal, and step function cases. These configurations are designed to mimic conditions of static, fast, and sudden changes in ion flows. The main results can be summarized as the following: (1) Vertical winds enhance dramatically at increasing spatial resolution along with increasing Joule heating primarily as a consequence of better resolving electric fields and larger relative ion-neutral flows; (2) Temporal variation and the magnitude of ion flows have a great impact on the vertical wind magnitude and temporal variability. Static ion flows lead to relatively small vertical winds with smaller variability. Sudden changes in ion flows produce much larger vertical winds with larger $\bar{\sigma}_{w_n}$ than fast changing ion flows.

[42] The thermospheric Joule or frictional heating is caused by a difference between the ion and neutral flow velocities in the presence of both ions and neutrals [*St.-Maurice and Schunk*, 1981; *Heelis and Coley*, 1988; *Vasyliūnas and Song*, 2005; *Yiğit and Ridley*, 2011]. The main contributions to Joule heating rate are then, the ion and neutral densities and flow velocities. Neutral winds play a significant role in shaping the variability of Joule heating [*Thayer*, 1998]. As pointed out in previous studies, there is also significant variability in the ion flow velocities that can appreciably enhance the Joule heating rate in the thermosphere. This is primarily caused because the forces that alter the ion flows are extremely strong compared to the forces that alter the neutral flows, while the total mass of the ions is quite small compared to the total mass of the neutrals. Therefore, the ion flows can change quite quickly over very short time periods, while the neutrals cannot. Indeed, studies have shown that the entire high-latitude ion flow patterns can change over a time-span of 10–15 min [*Ridley et al.*, 1998], while other studies have shown that the thermosphere takes approximately 3 hours to change [*Killeen et al.*, 1984].

[43] "Variability" of the ion flow has been discussed in different contexts by a number of authors. In one of the first studies of ionospheric flow variability by *Codrescu et al.* [2000], the ion flow variations within spatial and activity level bins were examined. This study, and similar studies, have argued that the variation within the bins can be interpreted as "variability". This may indeed be the case, but it may, in fact, not be the whole story. For example, the Codrescu study binned activity level by K_p, which is a 3-hour general indicator of activity level. If one were to examine a K_p bin of, for example, 3 near the dayside cusp region, there could be a wide variety of flows observed. This is not necessarily because the flows are highly variable, but because a K_p of 3 may include time periods in which there are strong B_y positive driven convection, B_y negative driven convection and B_y zero driven convection that vary significantly in terms of convection cell symmetry [e.g., *Weimer*, 1995]. This means that in a K_p 3 bin, the ion flows may be eastward, westward, or poleward. Hence, in such a bin, there will be a significant standard deviation. So, in some regards, the term "variability" in this case implies "uncertainty". An uncertainty in the ion flow velocity, while somewhat troubling, does not intrinsically lead to a larger Joule heating.

[44] Other models that take into account more parameters that control the ion flow, such as the *Weimer* [1996, 2001, 2005] models and other models that bin by IMF drive down the uncertainty due to the fact that they constrain the problem more, although these models do not necessarily drive down the uncertainty to zero. A study by *Bekerat et al.* [2003], showed that the model by *Weimer* [1996] only matches the ion flow approximately 5% of the time. Hence, there is still significant uncertainty. Utilizing a data

assimilation approach to the problem, *Kihn and Ridley* [2005] and *Bekerat et al.* [2005] showed that this uncertainty could be significantly reduced to approximately 30%.

[45] In addition to uncertainty, there is also the problem that the large-scale ionospheric convection pattern has sharp gradients. For example, when the IMF B_y is strong compared to B_z, there exists "banana" and "orange" cells. In the "banana" cell, there are very strong sheers in the flow. *Clauer and Ridley* [1995] and *Ridley and Clauer* [1996] showed that the convection reversal boundary in the "banana" cell can exist for long periods of time and can be extremely sharp. Models such as the *Weimer* [1996] model and the Assimilative Mapping of Ionospheric Electrodynamics (AMIE) technique [*Richmond and Kamide*, 1988], have resolutions that are larger than one degree, and so cannot hope to capture these sheers that may not have variability at all, but may just be small-scale. So, an additional aspect of the problem comes in the form of resolution - models are not able to capture the sharp, persistent, gradients that may exist in the ion flows. Just like uncertainty, this may not cause additional Joule heating to occur in the real world, but in models, the lack of sufficient resolution to properly capture standing gradients causes the Joule heating to be underestimated, as illustrated in the studies by *Deng and Ridley* [2007] and *Yiğit and Ridley* [2011].

[46] An additional aspect of ion flows is actual temporal variability. The study by *Ridley and Clauer* [1996] not only showed that strong sheers in the ion flow can exist in the convection reversal boundary, but that this boundary can become Kelvin Helmholtz unstable, such that the ion flows around the boundary vary dramatically on time-scales of tens of seconds. *Bristow* [2008] showed that the ion flows also vary rapidly over time-scales less than 10 min. Further, within the auroral zone, the ion flows and electron particle precipitation vary wildly in both time and space, especially when the activity level increases.

[47] Thermospheric and ionospheric models need to account for all of these things - both spatial and temporal variability across multiple scales. This is almost impossible to do, since models have limitations (e.g., resolution) in both the spatial and temporal domain.

[48] This study examines two aspects of this problem - spatial resolution, or resolving the standing ion flow patterns with higher resolution; and temporal variability, or examining what happens when the ion flows change rapidly. Specifically, this investigates the ramification of these two issues on the strength of the vertical wind speed in the thermosphere. In this study, it is shown that the vertical wind is extremely sensitive to both model resolution and temporal variability in the ion flows. The first part of the study shows that model resolution, or simply better capturing the peaks in the ion flow velocities, can increase the vertical winds in the thermosphere dramatically. This vertical wind is persistent, lasting for many hours, and is due to both the model's ability to capture the ion flows, enhancing the Joule heating, and the model's ability to better create strong convergences and divergences in the horizontal wind structure.

[49] The temporal variability of the ion flows, here modeled by rapidly changing the ionospheric cross polar cap potential, also significantly enhances the vertical winds. This enhancement occurs for two reasons: first, the difference between the relatively inert thermospheric winds and rapidly changing ion flows cause periods of enhanced Joule heating. Because the Joule heating is proportional to the square of the difference [*St.-Maurice and Schunk*, 1981], this is a nonlinear process [*Kirchengast*, 1997; *Yiğit and Ridley*, 2011], such that enhancing the difference has a much larger effect than diminishing the difference. So, when the ion flows are increased and decreased, the increase enhances the Joule heating more than the decrease reduces the Joule heating, such that the average is higher. The second reason is that when the Joule heating impulsively turns on, an acoustic wave is launched [*Deng et al.*, 2008], increasing the upward directed vertical winds. When the Joule heating turns off, an additional wave is launched, reversing the sign of the vertical wind. It is speculated that the more impulsive this energy source, the stronger the waves will be. This is demonstrated in the difference between the sin and square wave simulations - the square wave produced larger vertical winds that had significantly more variability. In the cases presented here, the electron density does not vary significantly between the model simulations with different ion flow variability due to our holding the solar extreme ultraviolet radiation and auroral activity constant. Thus, changes in electron density cannot contribute significantly to the variations in Joule heating seen in the different simulations.

[50] The investigation of the vertical acceleration demonstrates that plasma flow-induced high-latitude Joule heating can generate significant nonhydrostatic effects. This is due to strong localized heating causing an imbalance between the pressure gradient and gravity, which subsequently have a crucial impact on the magnitude and variability of the thermospheric vertical winds.

[51] The simulations that were conducted in this study are more for illustrative purposes than what would actually occur in the actual ionosphere and thermosphere. For example, as stated above, the global ionospheric convection pattern changes on time-scales of 10–15 min. With the square wave driver, the global convection changes in one minute, suddenly enhancing the Joule heating. While the global-scale ion flow should not change this dramatically in one minute, there are regions of the ionosphere in which the convection does change this rapidly, for example, near the convection reversal boundary [*Ridley and Clauer*, 1996], near the cusp [*Lanzerotti et al.*, 1991], and in the auroral zone on the night side. In these regions, the ion flows may vary dramatically in both space and time and so one would expect that there may exist significant, and highly variable, vertical winds, which is what is observed in reality [*Ishii et al.*, 2001; *Innis and Conde*, 2002]. In essence, what is needed are models of the ion flow velocity variability, not simply the uncertainty. If an understanding of how rapidly the ion flows change and where those changes maximize is achieved, we will better be able to describe the vertical motion of the thermosphere.

Appendix A: Nonhydrostatic Effects

[52] The hydrostatic equilibrium is given by the balance between the pressure and the gravitational force:

$$\frac{\partial p}{\partial r} = -\rho g, \tag{A1}$$

where p is pressure, r is the radial distance measured from the center of the Earth, ρ is mass density, and g is gravitational acceleration. Pressure is given by the ideal gas law:

$$p = nk_bT, \tag{A2}$$

where n is number density, and T is temperature, and k_b is Boltzmann constant. The hydrostatic balance equation can then be expressed in terms of n and T in the altitude coordinate system and using the relation $\rho = nm$, where ρ is mass density and m molecular mass, one obtains

$$\frac{1}{nm}\frac{\partial p}{\partial r} = \frac{1}{nm}\frac{\partial}{\partial r}(nk_bT) = \frac{k_b}{m}\frac{T}{n}\frac{\partial n}{\partial r} + \frac{k_b}{m}\frac{\partial T}{\partial r} = -g. \tag{A3}$$

If (A3) does not hold, it implies that the system is nonhydrostatic. In the Global Ionosphere Thermosphere Model (GITM), the vertical momentum equation is explicitly solved, for example, by accounting for neutral-neutral and ion-neutral momentum exchange, Coriolis and centrifugal effects, spherical geometry. Horizontal divergence can impact the $\partial n/\partial r$ and $\partial T/\partial r$ via continuity and thermodynamic energy relations, and can thus modify the extent of nonhydrostatic effects.

[53] **Acknowledgments.** This research has been funded by the following grants: NSF grants ANT0838828, ATM0640429, and ATM069336 and AFOSR grant FA9550-07-1-0434. The Global Ionosphere Thermosphere Model simulations have been performed using the computer facilities at the Department of Atmospheric and Oceanic and Space Sciences, University of Michigan.

[54] Robert Lysak thanks the reviewers for their assistance in evaluating this paper.

References

Bekerat, H. A., R. W. Schunk, and L. Scherliess (2003), Evaluation of statistical convection patterns for real-time ionospheric specifications and forecasts, *J. Geophys. Res.*, *108*(A12), 1413, doi:10.1029/2003JA009945.

Bekerat, H. A., R. W. Schunk, L. Scherliess, and A. Ridley (2005), Comparison of satellite ion drift velocities with AMIE derived convection patterns, *J. Atmos. Sol. Terr. Phys.*, *67*, 1463–1479, doi:10.1016/j.jastp.2005.08.013.

Biondi, M. A. (1984), Measured vertical motion and converging and diverging horizontal flow of the midlatitude thermosphere, *Geophys. Res. Lett.*, *11*, 84–87.

Bristow, W. (2008), Statistics of velocity fluctuations observed by SuperDARN under steady interplanetary magnetic field conditions, *J. Geophys. Res.*, *113*, A11202, doi:10.1029/2008JA013203.

Clauer, C. R., and A. J. Ridley (1995), Ionospheric observations of magnetospheric low-latitude boundary layer waves on August 4, 1991, *J. Geophys. Res.*, *100*(A11), 21,873–21,884.

Codrescu, M. V., T. J. Fuller-Rowell, J. C. Foster, J. M. Holt, and S. J. Cariglia (2000), Electric field variability associated with the Millstone Hill electric field model, *J. Geophys. Res.*, *105*(A3), 5265–5273.

Conde, M., and P. L. Dyson (1995), Thermospheric vertical winds above Mawson, Antarctica, *J. Atmos. Terr. Phys.*, *57*, 589–596.

Crickmore, R. I., J. R. Dudeney, and A. S. Rodger (1991), Vertical thermospheric winds at the equatorward edge of the auroral oval, *J. Atmos. Terr. Phys.*, *53*, 485–492.

Deng, Y., and A. J. Ridley (2007), Possible reasons for underestimating Joule heating in global models: E field variability, spatial resolution, and vertical velocity, *J. Geophys. Res.*, *112*, A09308, doi:10.1029/2006JA012006.

Deng, Y., A. D. Richmond, A. J. Ridley, and H. Liu (2008), Assessment of the non-hydrostatic effect on the upper atmosphere using a general circulation model (GCM), *Geophys. Res. Lett.*, *35*, L01104, doi:10.1029/2007GL032182.

Dickinson, R. E., E. C. Ridley, and R. G. Roble (1981), A three-dimensional general circulation model of the thermosphere, *J. Geophys. Res.*, *86*(A3), 1499–1512.

Fuller-Rowell, T. J., and D. S. Evans (1987), Height-integrated Pederson and Hall conductivity patterns inferred from TIROS-NOAA satellite data, *J. Geophys. Res.*, *92*(A7), 7606–7618.

Fuller-Rowell, T. J., and D. Rees (1980), A three dimensional time-dependent global model of the thermosphere, *J. Atmos. Sci.*, *37*, 2545–2567.

Hedin, A. E. (1991), Extension of the MSIS thermosphere model into the middle and lower atmosphere, *J. Geophys. Res.*, *96*(A2), 1159–1172.

Heelis, R. A. (1984), The effects of interplanetary magnetic field orientation on dayside high-latitude ionospheric convection, *J. Geophys. Res.*, *89*(A5), 2873–2880, doi:10.1029/JA089iA05p02873.

Heelis, R. A., and W. R. Coley (1988), Global and local joule heating effects seen by DE 2, *J. Geophys. Res.*, *93*(A7), 7551–7557.

Hernandez, G. (1982), Vertical motions of the neutral thermosphere at midlatitude, *Geophys. Res. Lett.*, *9*, 555–557.

Innis, J. L., and M. Conde (2001), Thermospheric vertical wind activity maps derived from Dynamics Explorer-2 WATS observations, *Geophys. Res. Lett.*, *28*, 3847–3850.

Innis, J. L., and M. Conde (2002), High-latitude thermospheric vertical wind activity from Dynamics Explorer 2 Wind and Temperature Spectrometer observations: Indications of a source region for polar cap gravity waves, *J. Geophys. Res.*, *107*(A8), 1172, doi:10.1029/2001JA009130.

Innis, J. L., P. A. Greet, D. J. Murphy, M. G. Conde, and P. L. Dyson (1999), A large vertical wind in the thermosphere at the auroral oval/polar cap boundary seen simultaneously from Mawson and Davis, Antarctica, *J. Atmos. Sol. Terr. Phys.*, *61*, 1047–1058, doi:10.1016/S1364-6826(99)00060-7.

Ishii, M., M. Conde, R. W. Smith, M. Krynicki, E. Sagawa, and S. Watari (2001), Vertical wind observations with two Fabry-Perot interferometers at Poker Flat, Alaska, *J. Geophys. Res.*, *106*(A6), 10,537–10,551.

Kihn, E. A., and A. J. Ridley (2005), A statistical analysis of the assimilative mapping of ionospheric electrodynamics auroral specification, *J. Geophys. Res.*, *110*, A07305, doi:10.1029/2003JA010371.

Killeen, T. L., and R. G. Roble (1984), An analysis of the high-latitude thermospheric wind pattern calculated by a thermospheric general circulation model: 1. Momentum forcing, *J. Geophys. Res.*, *89*(A9), 7509–7522.

Killeen, T. L., B. Hays, G. R. Carignan, R. A. Heelis, W. B. Hanson, N. W. Spencer, and L. H. Brace (1984), Ion-neutral coupling in the high-latitude F region: Evaluation of ion heating terms from Dynamics Explorer 2, *J. Geophys. Res.*, *89*(A9), 7495–7508.

Killeen, T. L., F. G. McCormac, A. G. Burns, J. P. Thayer, R. M. Johnson, and R. J. Niciejewski (1991), On the dynamics and composition of the high-latitude thermosphere, *J. Atmos. Terr. Phys.*, *53*, 797–815, doi:10.1016/0021-9169(91)90095-O.

Kirchengast, G. (1997), Characteristics of high-latitude TIDs from different causative mechanisms deduced by theoretical modeling, *J. Geophys. Res.*, *102*(A3), 4597–4612.

Kivanç, Ö., and R. A. Heelis (1998), Spatial distribution of ionospheric plasma and field structures in the high-latitude F region, *J. Geophys. Res.*, *103*(A4), 6955–6968.

Knipp, D. J., A. D. Richmond, B. Emery, N. U. Crooker, O. de la Beaujardiere, D. Evans, and H. Kroehl (1991), Ionospheric convection response to changing IMF direction, *Geophys. Res. Lett.*, *18*, 721–724.

Lanzerotti, L. J., R. M. Konik, A. Wolfe, D. Venkatesan, and C. G. Maclennan (1991), Cusp latitude magnetic impulse events: 1. Occurrence statistics, *J. Geophys. Res.*, *96*(A8), 14,009–14,022.

McHarg, M., F. Chun, D. Knipp, G. Lu, B. Emery, and A. Ridley (2005), High-latitude Joule heating response to IMF inputs, *J. Geophys. Res.*, *110*, A08309, doi:10.1029/2004JA010949.

Price, G. D., R. W. Smith, and G. Hernandez (1995), Simultaneous measurements of large vertical winds in the upper and lower thermosphere, *J. Atmos. Terr. Phys.*, *57*, 631–643.

Rees, D., R. W. Smith, P. J. Charleton, F. G. McCormac, N. Lloyd, and A. Kesteen (1984), The generation of vertical thermospheric winds and gravity waves at auroral latitudes—I. Observations of vertical winds, *Planet. Space Sci.*, *32*, 667–684, doi:10.1016/0032-0633(84)90092-8.

Richmond, A. D., and Y. Kamide (1988), Mapping electrodynamic features of the high-latitude ionosphere from localized observations: Technique, *J. Geophys. Res.*, *93*(A6), 5741–5759.

Richmond, A. D., E. C. Ridley, and R. G. Roble (1992), A thermosphere/ionosphere general circulation model with coupled electrodynamics, *Geophys. Res. Lett.*, *19*, 601–604.

Ridley, A. J., and C. R. Clauer (1996), Characterization of the dynamic variations of the dayside high-latitude ionospheric convection reversal boundary and relationship to interplanetary magnetic field orientation, *J. Geophys. Res.*, *101*(A5), 10,919–10,938.

Ridley, A. J., G. Lu, C. R. Clauer, and V. O. Papitashvili (1998), A statistical study of the ionospheric convection response to changing interplanetary magnetic field conditions using the assimilative mapping of

ionospheric electrodynamics technique, *J. Geophys. Res.*, *103*(A3), 4023–4039.
Ridley, A. J., Y. Deng, and G. Tóth (2006), The global ionosphere–thermosphere model, *J. Atmos. Sol. Terr. Phys.*, *68*, 839–864, doi:10.1016/j.jastp.2006.01.008.
Rishbeth, H. (1998), How the thermospheric circulation effects the ionospheric F2-layer, *J. Atmos. Sol. Terr. Phys.*, *60*, 1385–1402, doi:10.1016/S1364-6826(98)00062-5.
Roble, R. G., E. C. Ridley, and A. D. Richmond (1988), A coupled thermosphere/ionosphere general circulation model, *Geophys. Res. Lett.*, *15*, 1325–1328.
Sakanoi, T., and H. Fukunishi (1999), Observations of vertical winds in the thermosphere with a Fabry-Perot Doppler imager at Syowa station, *Adv. Space Res.*, *24*, 1439–1442.
Schmidt, H., G. P. Brasseur, M. Charron, E. Manzini, M. A. Giorgetta, T. Diehl, V. I. Fomichev, D. Kinnison, D. Marsh, and S. Walters (2006), The HAMMONIA chemistry climate model: Sensitivity of the mesopause region to the 11-year solar cycle and CO_2 doubling, *J. Clim.*, *19*, 3903–3931.
Smith, R. W. (1998), Vertical winds: A tutorial, *J. Atmos. Sol. Terr. Phys.*, *60*, 1425–1434, doi:10.1016/S1364-6826(98)00058-3.
Smith, R. W. (2000), The global-scale effect of small-scale thermospheric disturbances, *J. Atmos. Sol. Terr. Phys.*, *62*, 1623–1628, doi:10.1016/S1364-6826(00)00123-1.
Spencer, N. W., R. F. Theis, L. E. Wharton, and G. R. Carignan (1976), Local vertical motions and kinetic temperature from AE-C as evidence for aurora-induced gravity waves, *Geophys. Res. Lett.*, *3*, 313–316.
Spencer, N. W., L. E. Wharton, G. R. Carignan, and J. C. Maurer (1982), Thermosphere zonal winds, vertical motions and temperature as measured from dynamics explorer, *Geophys. Res. Lett.*, *9*, 953–956.
St.-Maurice, J.-P., and R. W. Schunk (1981), Ion-neutral momentum coupling near discrete high-latitude ionospheric features, *J. Geophys. Res.*, *86*(A13), 11,299–11,321.
Thayer, J. P. (1998), Height-resolved Joule heating rates in the high-latitude *E* region and the influence of the neutral winds, *J. Geophys. Res.*, *103*(A1), 471–487.
Thayer, J. P., and J. Semester (2004), The convergence of magnetospheric energy flux in the polar atmosphere, *J. Atmos. Sol. Terr. Phys.*, *66*, 807–824, doi:10.1016/j.jastp.2004.01.035.
Thayer, J. P., J. F. Vickrey, R. A. Heelis, and J. B. Gary (1995), Interpretation and modeling of the high-latitude electromagnetic energy flux, *J. Geophys. Res.*, *100*(A10), 19,715–19,728.
Vasyliūnas, V. M., and P. Song (2005), Meaning of ionospheric Joule heating, *J. Geophys. Res.*, *110*, A02301, doi:10.1029/2004JA010615.
Wardill, P., and F. Jacka (1986), Vertical motions in the thermosphere over Mawson, Antarctica, *J. Atmos. Terr. Phys.*, *48*, 289–292, doi:10.1016/0021-9169(86)90104-2.
Weimer, D. R. (1995), Models of high-latitude electric potentials derived with a least error fit of spherical harmonic coefficients, *J. Geophys. Res.*, *100*(A10), 19,595–19,607.
Weimer, D. (1996), A flexible, IMF dependent model of high-latitude electric potentials having "space weather" applications, *Geophys. Res. Lett.*, *23*, 2549–2552.
Weimer, D. R. (2001), An improved model of ionospheric electric potentials including substorm perturbations and application to the Geospace Environment Modeling November 24, 1996, event, *J. Geophys. Res.*, *106*(A1), 407–416.
Weimer, D. R. (2005), Improved ionospheric electrodynamic models and application to calculating Joule heating rates, *J. Geophys. Res.*, *110*, A05306, doi:10.1029/2004JA010884.
Wilson, G. R., D. R. Weimer, J. O. Wise, and F. A. Marcos (2006), Response of the thermosphere to Joule heating and particle precipitation, *J. Geophys. Res.*, *111*, A10314, doi:10.1029/2005JA011274.
Yiğit, E., and A. S. Medvedev (2009), Heating and cooling of the thermosphere by internal gravity waves, *Geophys. Res. Lett.*, *36*, L14807, doi:10.1029/2009GL038507.
Yiğit, E., and A. J. Ridley (2011), Effects of high-latitude thermosphere heating at various scale sizes simulated by a nonhydrostatic global thermosphere-ionosphere model, *J. Atmos. Sol. Terr. Phys.*, *73*, 592–600, doi:10.1016/j.jastp.2010.12.003.
Yiğit, E., A. D. Aylward, and A. S. Medvedev (2008), Parameterization of the effects of vertically propagating gravity waves for thermosphere general circulation models: Sensitivity study, *J. Geophys. Res.*, *113*, D19106, doi:10.1029/2008JD010135.
Yiğit, E., A. S. Medvedev, A. D. Aylward, P. Hartogh, and M. J. Harris (2009), Modeling the effects of gravity wave momentum deposition on the general circulation above the turbopause, *J. Geophys. Res.*, *114*, D07101, doi:10.1029/2008JD011132.

A. J. Ridley and E. Yiğit, Center for Space Environment Modeling, Department of Atmosphere, Oceanic and Space Sciences, University of Michigan, 1429 Space Research Bldg., 2455 Hayward St., Ann Arbor, MI 48109-2143, USA. (erdal@umich.edu)